PHYSICAL REVIEW D **94,** 023007 (2016)

High-energy electromagnetic cascades in extragalactic space: Physics and features

V. Berezinsky[1] and O. Kalashev[2]

[1]*INFN, Gran Sasso Science Institute viale F. Crispi 7, 67100 L'Aquila, Italy and Laboratori Nazionali del Gran Sasso, Assergi (AQ), 67010, Italy*

[2]*Institute for Nuclear Research of the Russian Academy of Sciences, Moscow 117312, Russia*

(Received 26 May 2016; published 19 July 2016)

Using the analytic modeling of the electromagnetic cascades compared with more precise numerical simulations, we describe the physical properties of electromagnetic cascades developing in the universe on cosmic microwave background and extragalactic background light radiations. A cascade is initiated by very-high-energy photon or electron, and the remnant photons at large distance have two-component energy spectrum, $\propto E^{-2}$ ($\propto E^{-1.9}$ in numerical simulations) produced at the cascade multiplication stage and $\propto E^{-3/2}$ from Inverse Compton electron cooling at low energies. The most noticeable property of the cascade spectrum in analytic modeling is "strong universality," which includes the standard energy spectrum and the energy density of the cascade $\omega_{\rm cas}$ as its only numerical parameter. Using numerical simulations of the cascade spectrum and comparing it with recent Fermi LAT spectrum, we obtained the upper limit on $\omega_{\rm cas}$ stronger than in previous works. The new feature of the analysis is the "$E_{\rm max}$ rule." We investigate the dependence of $\omega_{\rm cas}$ on the distribution of sources, distinguishing two cases of universality: the strong and weak ones.

DOI: 10.1103/PhysRevD.94.023007

I. INTRODUCTION

A very-high-energy extragalactic electron or photon colliding with low-energy background photons γ_t [cosmic microwave background (CMB) and extragalactic background light (EBL)] produces electromagnetic cascade due to reactions $\gamma+\gamma_t\to e^-+e^+$ [pair production (PP)] and $e+\gamma_t\to\gamma'+e$ [inverse Compton (IC) scattering]. Part of the cascade energy can be taken away by synchrotron radiation if the magnetic field is strong enough. The existence of such cascading was understood soon after discovery of CMB radiation [1] and of the Greisen-Zatsepin-Kuzmin cutoff[1] [2]. Since that time, electromagnetic (EM) cascading in extragalactic space has received many various applications.

One of the earliest applications was a rigorous upper limit on cosmogenic neutrino flux, which was proposed by Berezinsky and Zatsepin in 1969 [3]. The upper limit on this flux as was first obtained in Ref. [4], following from the observation that production of neutrinos and initial cascading particles (e and γ) takes place from the decay of the same particle, Δ^+ resonance, produced in $p\gamma_{\rm cmb}$ interaction, and thus the energy density of produced neutrinos and cascade particles are characterized by a ratio of $1/3$. A remarkable byproduct of this work was a good agreement of the analytically calculated cascade spectrum with a diffuse extragalactic gamma-ray spectrum as presented finally by the EGRET Collaboration in 1998 [5] in the range from 30 MeV to 130 GeV. The exponent of the EGRET spectrum $\alpha=2.1\pm0.03$ agrees quite well with that predicted in Ref. [4] as $\alpha=2.0$. The diffuse gamma-ray spectrum measured recently by Fermi-LAT [6,7] showed much worse agreement with the predicted cascade spectrum; in particular, the spectrum exponent is found to be $\alpha=2.3$. The allowed energy density of the cascade radiation is found to be [8]

$$\omega_{\rm cas}=5.8\times10^{-7}\ {\rm eV/cm^3}, \tag{1}$$

and it puts the severe limit on allowed flux of cosmogenic neutrinos and extragalactic protons in ultrahigh-energy cosmic rays (UHECRs) [8–10].

The new Fermi data [6] probably contradict also the more general early hypothesis that the extragalactic background gamma-ray flux observed by EGRET [5] and Fermi-LAT [6] is fully produced in $p\gamma$ interaction of extragalactic CRs followed by EM cascading. This hypothesis, put forward in the early 1970s, e.g., in Refs. [11] and [12], had the impact especially on the interpretation of the EGRET data, but the more complicated Fermi-LAT spectrum and in particular the discovery of discrete sources in the early background spectrum seriously questioned this interpretation.

Electromagnetic cascading strongly affected gamma astronomy of discrete sources. The first work in this field was calculation by Gould and Schreder [13] of the

[1]Oral remark by I. L. Rozental at Soviet-Union Cosmic Ray Conference, by personal recollection of one of us, VB, and independently by S. Hayakawa according to recollection of K. Sato.

absorption of gamma rays with energies above 100 TeV on CMB radiation in the Universe. Cascading of the absorbed photons was understood soon, and in 1970, the absorption of ultrahigh-energy (UHE) photons on optical, radio radiation, and in magnetic fields was included in the calculations, together with similar calculations for electrons [14].

The new step was done in the work by Aharanian *et al.* [15]. Before this work, a magnetic field in the cascading process was taken into account for energy losses of electrons and for absorption of photons in a very strong magnetic field. In the work [15], the authors noticed the importance of deflection of the cascade electrons in magnetic fields. In the absence of a magnetic field, cascade particles propagate from a source in the same direction as the parent photon. If an extragalactic magnetic field nearby the source is large enough, the low-energy cascade e^+e^--particles can be deflected from the direction of initial cascading photon and produce (by IC radiation) an isotropic low-energy $E_\gamma < 1$ TeV component named the "halo component" by the authors. As the sources, the AGN and in particular blazars are considered. In terms of presently estimated EBL radiation [16,17], the considered model looks as follows. An initial photon with energy $E_{\gamma 0} \sim 10$ TeV is absorbed on EBL with the mean absorption length $\ell_\gamma \sim 100$ Mpc, producing an electron and positron with energy $E_e \sim 5$ TeV each. the electron/positron is deflected in an extragalactic magnetic field producing then in IC scattering on a CMB photon the recoil photon with energy

$$E_\gamma^{\rm IC} \sim (4/3)\gamma_e^2 \varepsilon_{\rm cmb} \sim 100 \text{ GeV}, \quad (2)$$

where $\gamma_e = E_e/m_e$ is the Lorentz factor of the electron. Thus, a typical energy of halo radiation is $E \sim 100$ GeV, and the size of halo is $r_h \sim$ a few Mpc.

A very exiting application of cascading was started by the work of Neronov and Semikoz [18], who indicated a possibility to search for very weak seeds of magnetic fields in the Universe.

The creation of the seeds with extremely weak magnetic fields is a necessary part of the explanation of observed magnetic fields which can reach the tremendous values up to 10^{13} G deduced for pulsars. The strong magnetic fields can be produced very fast due to the collapse of the objects with a weak magnetic field and fast increasing of magnetic fields due to the dynamo mechanism. The problem is how the objects with very weak magnetic fields, the seeds, were produced. Two kinds of the seeds are in principle known: the cosmological and astrophysical ones (for reviews, see, e.g., Refs. [19–21] and the latest review with many references [22]). Magnetic seeds of astrophysical origin include historically the first model "Biermann battery" [23,24] and recently many models based on plasma instabilities, e.g., Ref. [25], and also on different models for Population III stars, e.g., Ref. [26].

To measure magnetic fields in seeds, Neronov and Semikoz [18] suggested observing the cascading propagation of TeV gamma rays from a source through a void with very weak magnetic fields. Secondary positrons and electrons are weakly deflected in magnetic fields producing thus extended emission of IC gamma rays, i.e., the gamma-ray halo described above. A decrease of the size of this halo with the energy of emitted gamma rays allows us to measure the strength of magnetic field B in a range 10^{-16} G $\lesssim B \lesssim 10^{-12}$ G [27].

At present, from the observation of cascading radiation of TeV gamma-ray sources (blazars), it became possible to put the lower limit on the extragalactic magnetic field [28]; for the review and other references, see Ref. [22].

Following the references cited above and observational data of the spectra of TeV blazars obtained by Fermi, one may explain an appearance of the lower limit on the extragalactic magnetic field in the following way.

Consider first the case $B = 0$ and gamma radiation from a blazar with primary energies higher than 1 TeV directed along the jet to an observer. These photons are absorbed, leaving behind the cascade radiation with low-energy spectra $\propto E^{-2}$ below cutoff and $E^{-1.5}$ at smaller energies (see Ref. [4] and Sec. II). These predicted low-energy spectra exceed the Fermi observation at $E \sim 1 - 100$ GeV, and the most natural assumption is the suppression of these fluxes due to the magnetic field, which deflects e^+e^- pairs from the direction to an observer. The Monte Carlo (MC) simulations from Refs. [28,29] and other calculations cited in Ref. [22] result in the lower bound $B > 10^{-17}$ G for extragalactic magnetic fields in voids. All these limits depend on the size of the coherence length of the magnetic field λ.

Apart from lower limits obtained using cascading from different blazars, there is one case of the positively measured magnetic field applying a quite different method suggested by T. Vachaspati and his collaborators [30,31] and references therein. This case is relevant for cascading in a helical magnetic field. Such a field scatters e^+e^- and provides a nonzero correlator between positions of three cascading gamma quanta produced by the IC radiation of electrons and positrons. The data of Fermi from blazars are used for the analysis. The helical magnetic field $B \sim 10^{-14}$ G is found on the 10 Mpc scale. This helical magnetic field can be produced in the early Universe at $t \sim 1$ ns.

Extragalactic magnetic fields in other structures, like filaments and galaxy clusters, are larger by many orders of magnitude, reaching the μG level in clusters. A reader can find a wider and more detailed discussion of extragalactic magnetic fields in the review [22]. Above, we limited ourselves by several issues connected with cascading.

This paper is organized in the following way. In Sec. II, we describe the cascade physics and obtain analytical solutions of cascade equations.

Our basic model in Sec. II is a static universe filled by background radiations with a dichromatic spectrum of photons with energy $\epsilon_{\rm cmb} = 6.3 \times 10^{-4}$ eV for CMB and $\epsilon_{\rm ebl} = 0.68$ eV for EBL radiation, the only free parameter in this model. Cascade is initiated by a very high-energy electron or photon with energy E_s and develops due to pair production $\gamma + \gamma_t \to e^+ + e^-$ and IC $e + \gamma_t \to e' + \gamma'$ scattering on background target photons γ_t. At large enough time, the spectrum of remnant photons obtains a *universal* form (independent from initial energy E_s, assuming E_s is high enough), which has universal characteristic energies: the energy of the spectrum cutoff

$$\mathcal{E}_\gamma^{\rm ebl} = \frac{m_e^2}{\epsilon_{\rm ebl}} = 3.9 \times 10^{11}\ {\rm eV}$$

and the energy of spectrum steepening

$$\mathcal{E}_X = \frac{1}{3}\mathcal{E}_\gamma^{\rm ebl}\frac{\epsilon_{\rm cmb}}{\epsilon_{\rm ebl}} = 1.2 \times 10^8\ {\rm eV}.$$

The spectrum of remnant photons is given by $n_\gamma(E) \propto E^{-3/2}$ at $E \le \mathcal{E}_X$, $n_\gamma(E) \propto E^{-2}$ at $\mathcal{E}_X \le E \le \mathcal{E}_\gamma$, and $n_\gamma(E) = 0$ at $E \ge \mathcal{E}_\gamma$.

The spectrum $n_\gamma(E) \propto E^{-3/2}$ at $E \le \mathcal{E}_X$ is robust. The spectrum at $\mathcal{E}_X \le E \le \mathcal{E}_\gamma$ is approximate: numerical simulation gives the exponent $\gamma = 1.9$ instead of 2.0. The cutoff is given in a rough approximation.

In Sec. II A, we demonstrate that the spectra obtained in the static universe using the analytic dichromatic model have the property of universality, which we will later call the strong universality. The main feature of the universal spectrum is its fixed shape, independent of initial energy E_s and distance to the source. The universality is broken for nearby sources.

In Sec. II B, the analytic universal spectrum is compared with numerical simulations for the cascades initiated at redshift z. For $z = 0.15$ (r = 626 Mpc), agreement for the dichromatic model with $\epsilon_{\rm ebl} = 0.68$ eV is good, as it is good for larger z but with the choice of different values of $\epsilon_{\rm ebl}$. The case of small distance (low z) needs a different treatment.

In Sec. II D, we consider physically and technically interesting cases of CMB-only radiation. This case is important at large z when the density of CMB photons strongly dominates and for nearby sources when absorption on EBL is small or absent. Technically, the case of CMB only is interesting because it automatically produces a dichromatic effect: the role of EBL photons is played by the photons with energy $\tilde{\epsilon}_{\rm cmb}$ from the high-energy tail of Planckian distribution, the density of which is enough to absorb a cascade photon with energy E of interest at considered distance r.

In this approximation, we calculated the cascade spectrum from nearby sources r = 1, 8.5, 85, and 200 Mpc and compared them with numerical simulations also with the assumption of CMB-only background radiation. The most noticeable difference with numerical simulation is observed at the smallest distance r = 1 Mpc because in realistic calculations the cascades arrive at an observer as underdeveloped with the spectrum $\propto E^{-1.47}$. The calculated parameters of the cascades are shown in Table I of Sec. II E. The new element of calculations is low-energy suppression of the spectrum shown by $\mathcal{E}_{\rm lec}^\gamma$ in Table I.

TABLE I. Parameters of analytic model for nearby sources (CMB only).

Distance r	1 Mpc	8.5 Mpc	85 Mpc	200 Mpc
$\tilde{\mathcal{E}}_\gamma$ eV	1.58×10^{14}	1.18×10^{14}	9.24×10^{13}	8.6×10^{13}
$\tilde{\epsilon}_{\rm cmb}$ eV	1.65×10^{-3}	2.21×10^{-3}	2.83×10^{-3}	3.04×10^{-3}
$\mathcal{E}_X$ eV	2.05×10^{13}	1.11×10^{13}	7.0×10^{12}	7.6×10^{12}
$\epsilon_{\rm cmb}$ eV	6.42×10^{-4}	6.24×10^{-4}	6.43×10^{-4}	8.0×10^{-4}
$\mathcal{E}_{\rm lec}^\gamma$ eV	4.34×10^8	6.01×10^6	6.01×10^4	1.09×10^4

In the Sec. III, we discuss the two numerical simulation techniques for the calculation of the cascade spectrum, namely, the solution of the one-dimension transport equation and Monte Carlo simulation. The former method is much faster and allows precise calculation of propagated spectra in the case in which cascade deflections are not important, while the latter method is good for investigating the effects of the magnetic field, e.g., in a problem of isotropization of the cascades emitted by point sources. We compare our numerically calculated spectra obtained with two techniques with each other and with independent numerical simulations.

In Sec. IV, the cases of strong and weak universality are introduced and discussed. In Sec. V, the corresponding spectra are calculated and compared with that measured by Fermi LAT. This comparison allows us to obtain upper limits on the energy density of the cascade radiation $\omega_{\rm cas}$, shown in Fig. 11 as function of production redshift. The limits are stronger for generations of the cascades at small redshifts.

In Sec. VI, we give a summary of the paper with the main conclusions. This section is written in an autonomous way and is designed for a reader who is interested in the main results and wants to bypass the technical details.

II. CASCADE PHYSICS AND ANALYTIC CALCULATIONS

We develop here a simplified model for the cascade which allows us to obtain an approximate spectrum of sterile (remnant) photons left behind after the cascade multiplication. We perform the approximate calculations of the EM cascade from a burst of radiation in the form of very-high-energy electrons or photons at a very large distance from an

observer. One may think of a single electron or photon with very-high-energy $E_s \gtrsim 10^{15}$ eV or a number of such particles. We use the *dichromatic spectrum* of background radiation which consists of photons with energy $\epsilon_{\rm cmb}$ and $\epsilon_{\rm ebl}$, analogs of CMB and extragalactic background light EBL with fixed energies of orders of 6.3×10^{-4} eV and $\sim$1 eV, respectively. We assume $\epsilon_{\rm ebl} \gg \epsilon_{\rm cmb}$ for energies and $n_{\rm cmb} \gg n_{\rm ebl}$ for space densities. A cascade is initiated by a single electron or photon with very-high-energy E_s and proceeds through PP, $\gamma + \gamma_{\rm bckgr} \to e^- + e^+$, and IC scattering, $e + \gamma_{\rm bckgr} \to e' + \gamma'$, on low-energy background photons (CMB or EBL). We assume a low magnetic field, which does not influence the cascade development due to synchrotron radiation, and our calculations will be mostly concerned with the mean diffuse photon flux which is not affected by deflections of the cascade electrons and positrons in the magnetic field.

We consider first the flat static universe and calculate the cascade spectrum from a pointlike burst of radiation at a large distance from an observer. The remnant cascade photons at large distances become cascade sterile, and we refer to the spectrum of these photons as universal.

To compare the calculated spectrum with numerical simulations, we further consider the expanding universe and a burst of high-energy radiation at a point with redshift z. In this case, the spectrum of sterile photons remaining from the EM cascade undergoes the redshift.

A. Universal spectrum in analytic calculations

In this subsection, we consider the flat static universe and EM cascade from a pointlike burst of very-high-energy photons or electrons at distances from an observer to be large enough for remnant photons to become sterile.

The criterion of high energy (HE) and low energy (LE) for a cascade particle with energy E is given with help of dimensionless parameter x_t,

$$x_t = E\varepsilon_t/m_e^2, \tag{3}$$

where ε_t is the energy of a target photon (t = CMB or EBL). $x_t \gg 1$ and $x_t \ll 1$ characterizes HE and LE regimes, respectively. In the HE regime, for both PP and IC, a cascade particle propagates as a leading particle $\gamma \to e \to \gamma \to e$ (see Fig. 1, leading-particle

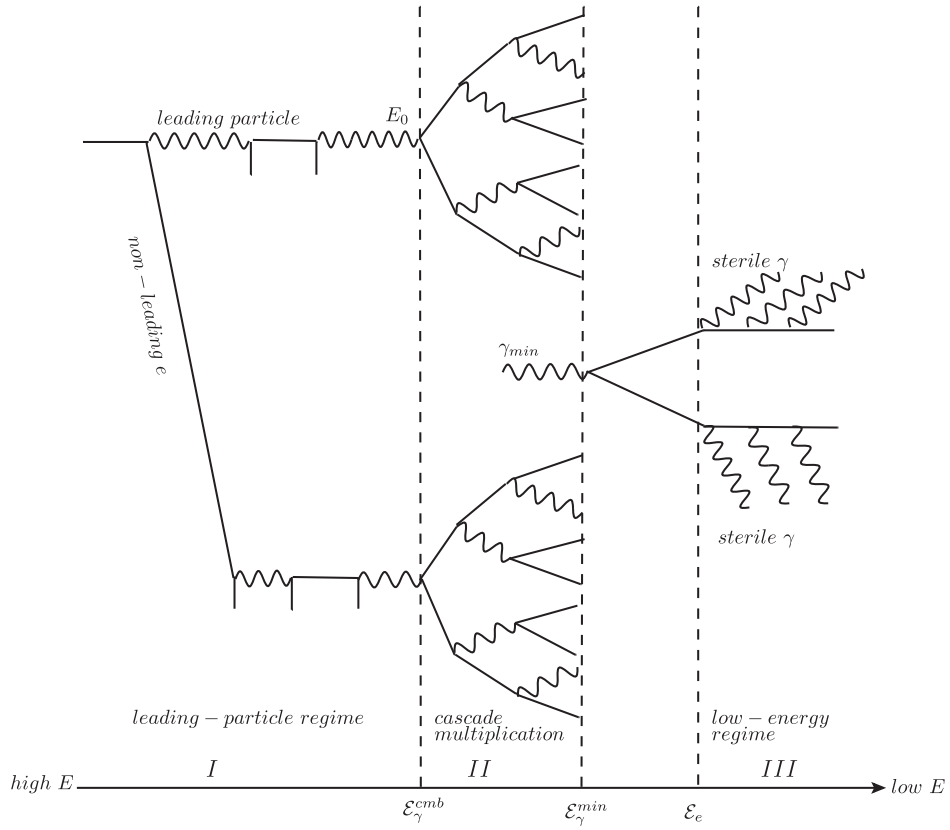

FIG. 1. Qualitative picture of the cascade development in the static universe for monoenergetic energies of background photons $\epsilon_{\rm cmb}$ and $\epsilon_{\rm ebl}$ with the assumption $\epsilon_{\rm ebl} \gg \epsilon_{\rm cmb}$ and $n_{\rm cmb} \gg n_{\rm ebl}$. The energies of cascade particles $\mathcal{E}_\gamma^{\rm cmb}$, $\mathcal{E}_\gamma^{\rm min}$, and $\mathcal{E}_e$ mark three regions of the cascade development: (I) HE leading-particle regime when a leading particle loses very small energy in a collision with background photons; (II) fast cascade multiplication, with a comparable fraction of energy obtained by each of two produced particles; and (III) regime of production of sterile photons by the electrons with energy $E \le \mathcal{E}_e$ (see the text for details.)

regime) losing in each collision (PP and IC) a fraction of energy [14]:

$$f \approx 1/[\ln(2E\varepsilon/m_e^2)]. \quad (4)$$

The turning point occurs when a leading particle approaches $x \gtrsim 1$ and enters *multiplication regime* II in Fig. 1.

In the case of an expanding universe, we assume that development of the cascade occurs during time $\tau_{\rm cas}(E)$, much shorter than the Hubble time $H^{-1}(z_b)$, where $\tau_{\rm cas}(E) \sim 1/(\sigma(E) c n_{\rm bckgr})$ and $\sigma(E)$ is a cross section for the HE photon or electron. The cascade development continues until the cascade photons reach, due to multiplication, the threshold of pair production in the process $\gamma + \gamma_{\rm ebl} \to e^+ + e^-$. After this moment, the remnant cascade photons lose energy only by redshift.

Because of inequality $n_{\rm cmb} \gg n_{\rm ebl}$, the cascade development proceeds in two stages. In the first one, a cascade develops in collisions with CMB photons only: $\gamma + \gamma_{\rm cmb} \to e^- + e^+$ and $e + \gamma_{\rm cmb} \to e' + \gamma'$. At the second stage, the remnant photons from the HE part of the distribution are absorbed on EBL radiation $\gamma + \gamma_{\rm ebl} \to e^- + e^+$, and then the produced e^+ and e^- are scattered on more numerous CMB photons: $e + \gamma_{\rm cmb} \to e' + \gamma'$. Because of this, calculations of the cascade on the CMB background only has the physical importance. This stage becomes particularly significant at $z_b \gg 1$ when the EBL radiation is absent and a cascade develops only on CMB. At smaller readshifts, EBL radiation appears, and the cascade enters its second stage.

The remnant photon spectrum is characterized by the following benchmark energies: the minimum energy of the absorbed photon $\mathcal{E}_\gamma^{\rm min}$, which we refer to as *min-photon*; the minimum energy of absorbed photons for CMB background only $\mathcal{E}_\gamma^{\rm cmb}$; the minimum energy of the cascade electron/positron $\mathcal{E}_e = \mathcal{E}_\gamma^{\rm min}/2$ (*min-electron*); and the energy $\mathcal{E}_X$ of the photon (*X-photon*) produced in IC scattering by min-electron. These energies are listed below in Eq. (5) together with their numerical values estimated for values $\epsilon_{\rm cmb} = 6.3 \times 10^{-4}$ eV and $\epsilon_{\rm ebl} = 0.68$ eV (see the discussion below):

$$\begin{aligned}
\mathcal{E}_\gamma^{\rm min} &= \mathcal{E}_\gamma^{\rm ebl} = \frac{m_e^2}{\epsilon_{\rm ebl}} = 3.9 \times 10^{11}\ {\rm eV} \\
\mathcal{E}_\gamma^{\rm cmb} &= \frac{m_e^2}{\epsilon_{\rm cmb}} = 4.1 \times 10^{14}\ {\rm eV} \\
\mathcal{E}_e &= \frac{1}{2}\mathcal{E}_\gamma^{\rm min} = 1.95 \times 10^{11}\ {\rm eV} \\
\mathcal{E}_X &= \frac{1}{3}\mathcal{E}_\gamma^{\rm min}\frac{\epsilon_{\rm cmb}}{\epsilon_{\rm ebl}} = 1.2 \times 10^{8}\ {\rm eV}
\end{aligned} \quad (5)$$

These energies appear in the cascade development illustrated by Fig. 1.

At the highest energies $x \gg 1$, the cascade develops in a leading particle regime I, $\gamma \to e \to \gamma \to e$, with a small fraction of energy (4) lost in every collision. The nonleading particle in this process is always the electron (or positron). However, as long as $E_e^{\rm nl}\varepsilon/m_e^2 \gg 1$, the nonleading electron propagates as a leading particle and transfers its energy to cascade multiplication regime II (see Fig. 1, leading-particle regime I). As numerical calculations show, the total energy injected into regime II approximately equals the initial energy E_s, mainly because the nonleading electrons can enter the multiplication regime (see Fig. 1).

The leading-particle regime finishes at $\mathcal{E}_\gamma^{\rm cmb}$, when e^+e^- pairs are not produced on CMB photons, and approximately at this energy cascade multiplication regime II starts. Pair production there occurs on EBL radiation, while IC scattering proceeds mainly on more numerous CMB photons. The minimum energy $\mathcal{E}_\gamma^{\rm min} = 3.9 \times 10^{11}$ eV of photons, which are able to produce e^+e^- pairs on high-energy EBL target photons, mark the end of the cascade multiplication and the beginning of low-energy region III where IC scattering on CMB photons, $e + \gamma_{\rm cmb} \to e' + \gamma'$, dominates. The produced photons are cascade sterile and, in consideration of this subsection, propagate losing the energy only adiabatically.

The energy spectrum of these photons is easy to calculate from two relations, $dn_\gamma = dE_e/E_\gamma$ and $E_\gamma \approx (E_e/m_e)^2\epsilon_{\rm cmb}$, valid for low-energy regime III. One obtains

$$dn_\gamma/dE_\gamma \propto E_\gamma^{-3/2}. \quad (6)$$

Equation (6) gives the robust prediction for low-energy asymptotics of the cascade spectrum.

There is one feature common for all stages of cascades I–III: due to the strong dominance of the density of CMB photons, $n_{\rm cmb} \gg n_{\rm ebl}$, IC scattering is always dominated by CMB photons.

For this regime in region III and most of region II, the relation given by Eq. (7) is valid,

$$E'_\gamma = \frac{4}{3}\gamma_e^2\epsilon_{\rm cmb}, \quad (7)$$

where $\gamma_e = E_e/m_e$ is the electron Lorentz factor and E'_γ is the average energy of the CMB photon after scattering off the electron. This equation was obtained in Refs. [32] and [14], and it is valid at the energy of target photons $\varepsilon_r \ll m_e$ in the system where the electron is at rest.

The essential feature of Eq. (7), $E'_\gamma \sim \gamma_e^2\epsilon_{\rm cmb}$, can be easily obtained from the Lorentz transformations. Indeed, consider an electron with Lorentz factor γ_e colliding with CMB photon $\epsilon_{\rm cmb}$. The energy of this target photon in the rest frame system of the electron, $\epsilon_r \sim \gamma_e\epsilon_{\rm cmb}$, is assumed to

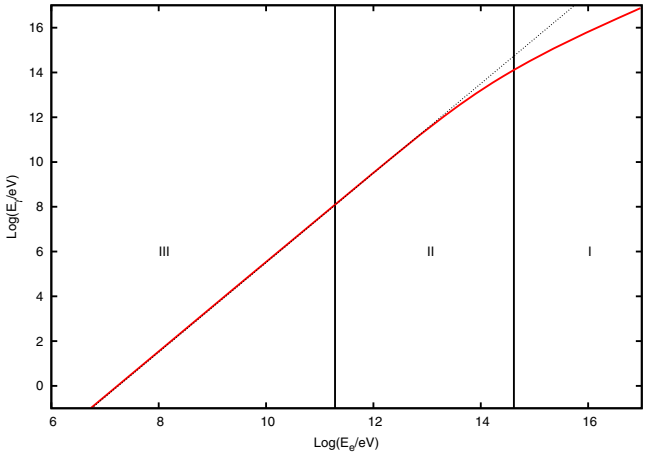

FIG. 2. Comparison of the exact calculation of the mean energy of the recoil CMB photon E'_γ in IC scattering (shown by the red curve) and its asymptotic dependence according to Eq. (7) (black dotted line).

be much smaller than m_e. After scattering, such a photon does not change its energy $\epsilon'_r = \epsilon_r$, and in the laboratory system, it is typically boosted by another Lorentz factor γ_e: $\epsilon' \sim \gamma_e \epsilon'_r \sim \gamma_e^2 \epsilon_{\rm cmb}$. In Fig. 2, we compare E'_γ from Eq. (7) (black dotted line) with exact calculation (red line), both given as a function of electron energy E_e plotted at the abscissa. One may see that maximum energy E'_γ from Eq. (7) is valid up to 3×10^{13} eV. In fact, in all cases where we apply Eq. (7), the maximum energy of photon spectra is limited by absorption on EBL radiation $\mathcal{E}_\gamma^{\rm ebl} = \frac{m_e^2}{\epsilon_{\rm ebl}} = 3.9 \times 10^{11}$ eV, which is well below 3×10^{13} eV allowed by exact calculations. The only almost exceptional case $\mathcal{E}_X = 2.0 \times 10^{13}$ eV is given by nearby sources (see Table I in Sec. II E). The flat $\propto E^{-1.7}$ part of the spectrum between $\mathcal{E}_X$ and $\mathcal{E}_\gamma$ is a reflection of more flat red curve in Fig. 2 above $E'_\gamma = 3 \times 10^{13}$ eV.

It is important to note that, instead of following the time-dependent cascade development, we consider a history of a cascade in terms of *particle generations*. Particles, electrons, and photons can reach given generation ν at different times. The total number of particles in one generation is $N_{\rm tot} = 2^\nu$, and the relation between the number of electrons N_e and photons N_γ in the same generation with large ν is approximately $N_e \approx 2N_\gamma$ [in case a cascade starts by an electron, this relation is given by $N_e = 2N_\gamma + (-1)^\nu$, and in case it starts by a photon, $N_e = 2N_\gamma - 2(-1)^\nu$].

For calculation of the cascade energy spectrum, we introduce the quantity $q(E)$, as a number of cascade particles passing through energy E during the whole time of cascade propagation. For electrons and photons, we use notation $q_e(E)$ and $q_\gamma(E)$, respectively. Assuming that the total energy in the cascade is conserved, one can use the equality of primary-particle energy E_s and the total energy $E \times q(E)$ which flows through energy E during all the cascade history. Taking into account that $N_e \approx 2N_\gamma$ in each generation of the cascade in multiplication region II, one obtains $q_e(E) = (2/3)E_s/E$ and $q_\gamma(E) = (1/3)E_s/E$ (for a different way to prove $q(E) \propto (1/E)$, see Refs. [4] and [33]). For low-energy regime III, we have $q_e(E) = {\rm const}$ for electrons and $q_\gamma(E)$ increasing with energy due to the low-energy tail of photons produced by electrons.

The basic equation for the number of the cascade photons $n_\gamma(E)$ reads

$$dn_\gamma(E_\gamma) = q_e(E_e) dE_e / E_\gamma. \tag{8}$$

In low-energy regime III in addition to Eq. (8) we assume constant electron flux $q_e(E_e) = q_0$ at $E_e \le \mathcal{E}_e$ and use aproximate relation $E_\gamma \propto E_e^2$ for IC photon production on CMB photons. It results in $dn_\gamma/dE_\gamma \propto E_\gamma^{-3/2}$ at $E_\gamma \le \mathcal{E}_X$ in agreement with Eq. (6).

In multiplication regime II in addition to the basic equation (8) we again use aproximate relation $E_\gamma \propto E_e^2$ while for electron flux we assume $q_e(E_e) \propto 1/E_e$. We obtain thus $dn_\gamma/dE_\gamma \propto E_\gamma^{-2}$, valid in the interval $\mathcal{E}_X \le E_\gamma \le \mathcal{E}_\gamma^{\rm min}$. At $E_\gamma \ge \mathcal{E}_\gamma^{\rm min}$, all remnant photons are absorbed, and $dn_\gamma/dE_\gamma = 0$.

Thus, we finally obtain for the spectrum of remnant photons in terms of the total number of particles n_γ,

$$n_\gamma(E_\gamma) = \begin{cases} (K/\mathcal{E}_X)(E_\gamma/\mathcal{E}_X)^{-3/2} & \text{at } E_\gamma \le \mathcal{E}_X \\ (K/\mathcal{E}_X)(E_\gamma/\mathcal{E}_X)^{-2} & \text{at } \mathcal{E}_X \le E_\gamma \le \mathcal{E}_\gamma \\ 0 & \text{at } E_\gamma > \mathcal{E}_\gamma, \end{cases} \tag{9}$$

where absorption energy $\mathcal{E}_\gamma = \mathcal{E}_\gamma^{\rm min} = m_e^2/\varepsilon_{\rm ebl} = 3.9 \times 10^{11}$ eV is the minimum energy of the absorbed photon (min-photon) and transition energy $\mathcal{E}_X = (4/3)(\mathcal{E}_e/m_e)^2 \varepsilon_{\rm cmb} = 1.2 \times 10^8$ eV is the energy of the IC photon radiated by min-electron produced in the absorption of the min-photon. Everywhere below, we use $\mathcal{E}_\gamma$ and $\mathcal{E}_X$ as generic notation for the cutoff energy and energy of transition between $E^{-3/2}$ and E^{-2} regimes, respectively. The background radiation (CMB or EBL) can be indicated as indices, when it is needed. The normalizing coefficient K can be found from the conservation of energy in the cascade, with the total energy equal to energy E_s of the primary electron or photon,

$$K = \frac{E_s}{\mathcal{E}_X(2 + \ln \mathcal{E}_\gamma/\mathcal{E}_X)}. \tag{10}$$

We will refer to spectrum (9) with normalization (10) as the *universal spectrum*: its shape is fixed independently on initial energy E_s or even injection spectrum $Q(E_s)$, if initial energy is sufficiently high, larger than scale energy E_0, which can be taken as $\mathcal{E}_\gamma^{\rm cmb}$ from Eq. (5).

The initial energy E_s (or energy density $\omega_{\rm cas}$ for the diffuse flux) changes only total normalization coefficient K from Eq. (10). Thus, the shape of the cascade spectrum does not depend on the injection spectrum and propagation time (the spectrum is frozen at the remnant-photons stage and forgets about its production stage). This universality will be referred to as "strong universality."

The universal spectrum given by Eq. (9) with normalization (10) has been obtained above in the simple model for a static flat universe, but in fact it is valid for a wide class of different models, e.g., for a realistic expanding universe at fixed redshift, if cascade develops at time τ shorter than the Hubble time $H^{-1}(z)$. In many cases below, Eqs. (9) and (10) are valid, though with numerical values of $\mathcal{E}_\gamma$, $\mathcal{E}_X$, and K different from that given above.

The universal spectrum of remnant photons left behind from the cascading of particles on dichromatic background photons with energies $\varepsilon_{\rm cmb} = 6.3 \times 10^{-4}$ eV and $\varepsilon_{\rm ebl} = 0.68$ eV in a flat universe at a large distance from an observer is characterized by the following spectral features: it has a flat energy spectrum $\propto E_\gamma^{-3/2}$ from the lowest energies and up to $\mathcal{E}_X = 1.2 \times 10^8$ eV, and it becomes more steep $\propto E^{-2}$ at higher energies, followed by a sharp cutoff at $\mathcal{E}_\gamma = m_e^2/\varepsilon_{\rm ebl} = 3.9 \times 10^{11}$ eV due to absorption on EBL photons. The most reliable predictions of this simple model are the low-energy spectral shape $\propto E^{-3/2}$ (robust) and cascade-multiplication one $\propto E^{-2}$ (probably approximate), while prediction of the sharp cutoff at $\mathcal{E}_\gamma$ is caused by the assumption of the large distance to the source and monochromatic spectrum of EBL. The sharpness of the spectral feature at $\mathcal{E}_X$ with its numerical value is an artifact of the dichromatic model of background radiation. In fact, at both energies $\mathcal{E}_X$ and $\mathcal{E}_\gamma$, there must be the transition regions.

The low-energy component of spectrum (9) $\propto E^{-1.5}$ is a signature of low-energy IC scattering (7), while the component $\propto E^{-2}$ is a signature of the cascade multiplication (region II in Fig. 1 up to the cutoff at energy $\mathcal{E}_\gamma^{\rm ebl} = 3.9 \times 10^{11}$ eV).

Equation (9) gives the total number of photons from a pointlike source. In particular, in the case of one primary UHE photon/electron, $n_\gamma(E_\gamma)dE_\gamma$ gives the total number of the cascade photons with energy E_γ observed at any large distance r from a source. Since both the characteristic energies $\mathcal{E}_\gamma$ and $\mathcal{E}_X$ do not depend on distance and energy E_s, Eq. (9) presents the same universal spectrum $n_\gamma(E_\gamma)$ for any initial energy E_s being larger than energy $\mathcal{E}_\gamma$. Equation (9) gives also *diffuse flux* with normalization E_s substituted by the energy density of the cascade radiation $\omega_{\rm cas}$. Since the cascade spectra $n_\gamma(E_\gamma)$ are the same far all E_s (apart from the total normalization), the spectra are the same for any generation spectrum $Q_g(E_s)$. In other words, the resultant universal spectrum forgets about its parent generation spectrum.

The diffuse flux of the cascade radiation is described by the space density of the cascade photons $n_\gamma(E_\gamma)$ with normalization given by Eq. (10), where E_s is substituted by the energy density $\omega_{\rm cas}$. The problem here is an additional component at $E_\gamma > \mathcal{E}_\gamma$ due to nearby sources (see Sec. II E).

In conclusion, the universality of spectrum (9) for both remote pointlike sources and diffuse radiation implies that all characteristics of the spectrum do not depend on the primary energy E_s and distance r (for a pointlike source). The universal spectrum, obtained above in a static universe, describes in fact a rather wide class of remote gamma-ray sources in the universe and also diffuse gamma-ray radiation. In the next subsections, Secs. II B, II C, and II E, we will present the relevant comparison with numerical simulations for pointlike sources and discuss the phenomena which limit the validity of the universal spectrum.

B. Comparison of universal spectrum with numerical simulations

In this subsection, we compare the universal spectrum, obtained within our simplified model, with realistic numerical simulation. The universal spectrum (9) is not valid for sources at too small and too large redshifts z. At small redshifts (nearby sources), absorption on EBL, which is an essential feature of our model, may not occur because of the small distance and low space density of EBL photons. Cascades may not be produced at all if a primary photon has energy E_s less than the threshold of pair production on EBL, $\mathcal{E}_\gamma$.

Note that in our calculations we did not include at all the density of target photons. Instead, we just assumed that the distance to a source is large enough for photon absorption at $E > \mathcal{E}_\gamma$.

For nearby sources, this assumption fails. In the case of low-density $n_{\rm ebl}$ of EBL photons, $\sigma_{\rm pair} n_{\rm ebl} r_{\rm source} \ll 1$, a cascade may still develop on CMB only, and this case will be considered below. Even if a photon is absorbed, the cascade still may not develop. It happens when the characteristic IC radiation length for the secondary electron/positron exceeds the distance to the observer.

At the large redshits z, comparison with numerical simulations may fail, because in analytic calculations we neglect the effects of the universe expansion and energy redshift. We will include these effects in the next subsection and thus extend our consideration to larger redshifts. The first comparison of analytic calculations [34] (similar to our static-universe model) with MC simulation for sources with fixed redshift z was done in Ref. [35] and is presented in the upper panel of Fig. 3. We can compare now the predicted spectrum (9) shown by the thick black line, with the MC spectrum from Ref. [35]. For $z = 0.15$ ($r = 626$ Mpc), we see the good agreement with the model where the energy of EBL photons is fixed as $\varepsilon_{\rm ebl} = 0.676$ eV. The low-energy spectrum $\propto E^{-1.5}$ is reliably confirmed. The cascade

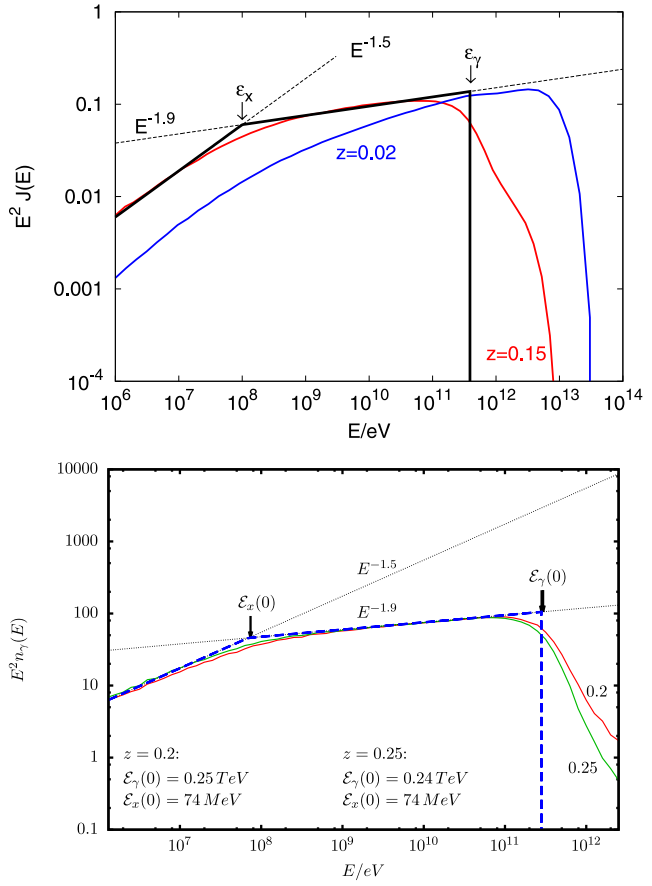

FIG. 3. Comparison of analytic calculations (black thick line) with numerical simulation (red and blue lines for $z = 0.15$ and $z = 0.02$ correspondingly from the work by Kachelrieß *et al.* [35] (*upper panel*) and from the present work (*lower panel*) for redshifts $z = 0.2$ (red line) and 0.25 (green line). Analytic calculations in the lower panel are presented by blue broken lines. For both panels, the line $\propto E^{-1.5}$ is shown for comparison; the characteristic energies in analytic calculations $\mathcal{E}_X$ and $\mathcal{E}_\gamma$ are shown by arrows (see the text).

multiplication spectrum ($\propto E^{-2}$) is seen as $E^{-1.9}$. Values of $\mathcal{E}_X$ and $\mathcal{E}_\gamma$ agree well with MC simulation. The MC simulation gives a smooth transition between different regimes, while in analytic calculations, it is sharp because of the dichromatic spectrum of the background.

For $z = 0.02$ ($r = 83.4$ Mpc), agreement is bad, and it has to be interpreted as a small distance to the source.

In the lower panel of Fig. 3, the analytic spectrum (9) is compared with our numerical simulations with the same conclusions (see Sec. III).

The success of the static model is provided by a large, but not too large, value of z. For larger redshifts, we have to generalize our analytic calculations for an expanding universe.

C. Expanding universe and comparison for $z > 0.3$

For large redshifts $z > 0.3$, we assume that cascades have enough time to develop during the Hubble time $H^{-1}(z)$ into the spectrum given by Eq. (9). The energies of background photons at epoch z are assumed to be $\varepsilon_{\rm cmb}(z) = (1+z)\varepsilon_{\rm cmb}$ for CMB and $\varepsilon^z_{\rm ebl} > \varepsilon_{\rm ebl}$ for EBL. Accordingly, the characteristic energies at redshift z become $\mathcal{E}_\gamma(z) = m_e^2/\varepsilon^z_{\rm ebl}$ and $\mathcal{E}_X(z) = \frac{1}{3}(\mathcal{E}_\gamma(z)/m_e)^2\varepsilon_{\rm cmb}(z)$. The spectrum of remnant photons at epoch z, $n_\gamma(E_\gamma, z)$, is given by Eq. (9) with $\mathcal{E}_X \equiv \mathcal{E}_X(z)$ and $\mathcal{E}_\gamma \equiv \mathcal{E}_\gamma(z)$. At the propagation of this spectrum to $z = 0$, the energies of photons E_γ and characteristic energies $\mathcal{E}_\gamma(z)$ and $\mathcal{E}_X(z)$ are redshifted by factor $(1+z)$, but Eq. (9) remains the same with the invariant value of K provided by the conservation of the number of particles during the redshift process, $n_\gamma(E_\gamma, z)dE_\gamma = n_\gamma(E, 0)dE$. Redshifted characteristic energies are given by

$$\mathcal{E}_\gamma(0) = \frac{m_e^2}{\varepsilon^z_{\rm ebl}}\frac{1}{1+z}, \qquad \mathcal{E}_X(0) = \frac{m_e^2\varepsilon_{\rm cmb}}{3(\varepsilon^z_{\rm ebl})^2}. \tag{11}$$

From the second relation in Eq. (11), one finds the energy of the EBL photon $\varepsilon^z_{\rm ebl}$ at epoch z as

$$\varepsilon^z_{\rm ebl} = \left(\frac{m_e^2\varepsilon_{\rm cmb}}{3\mathcal{E}_X(0)}\right)^{1/2}. \tag{12}$$

Now, the procedure of comparing the analytic solution with the numerical simulation consists of the following four operations illustrated by Fig. 4:

(i) Normalization of the $E^{-1.5}$ part of the analytic solution by the $E^{-1.5}$ part of the simulation.
(ii) Finding $\mathcal{E}_X(0)$ as the intersection of the $E^{-1.5}$ and $E^{-1.9}$ parts of the spectrum (see Fig. 4). In this operation, we neglect the difference between $E^{-1.9}$ and E^{-2}.
(iii) Calculation of $\varepsilon^z_{\rm ebl}$ using Eq. (12).
(iv) Calculation of cutoff energy $\mathcal{E}_\gamma(0)$ from Eq. (11).

A comparison of the analytic solutions with numerical simulation is presented in Fig. 4 for redshifts $z = 0.32$, 0.4, 0.64, 1.0. The analytic solution predicts that the cascade spectrum consists of two power-law components $E^{-1.5}$ and E^{-2}, with the intersection at $\mathcal{E}_X$. The numerical simulations confirm this prediction with component $E^{-1.9}$ instead of E^{-2}. The only free parameter in the analytic calculations is the energy of EBL photons for each redshift, which means the value of $\varepsilon_{\rm ebl} \approx 0.68$ at $z = 0$ and evolution $\varepsilon^z_{\rm ebl}/\varepsilon_{\rm ebl} = f(z)$. The free parameter $\varepsilon^z_{\rm ebl}$ determines two characteristic energies $\mathcal{E}_X$ and $\mathcal{E}_\gamma$.

In contrast to the sharp spectral features in analytic calculations, the numerical simulations predict a smooth transition regime centered by these features.

The evolution of EBL energy $\varepsilon^z_{\rm ebl}/\varepsilon_{\rm ebl}$ with z in a dichromatic model must correspond, to some extent, to the evolution of the mean EBL energy $\bar{\varepsilon}_{\rm ebl}(z)$ with redshift.

The numerical simulations show an interesting feature of merging the spectrum $n_\gamma(E, z)$ to $E^{-1.9}$ at increasing z, which coincides within the accuracy of calculations with

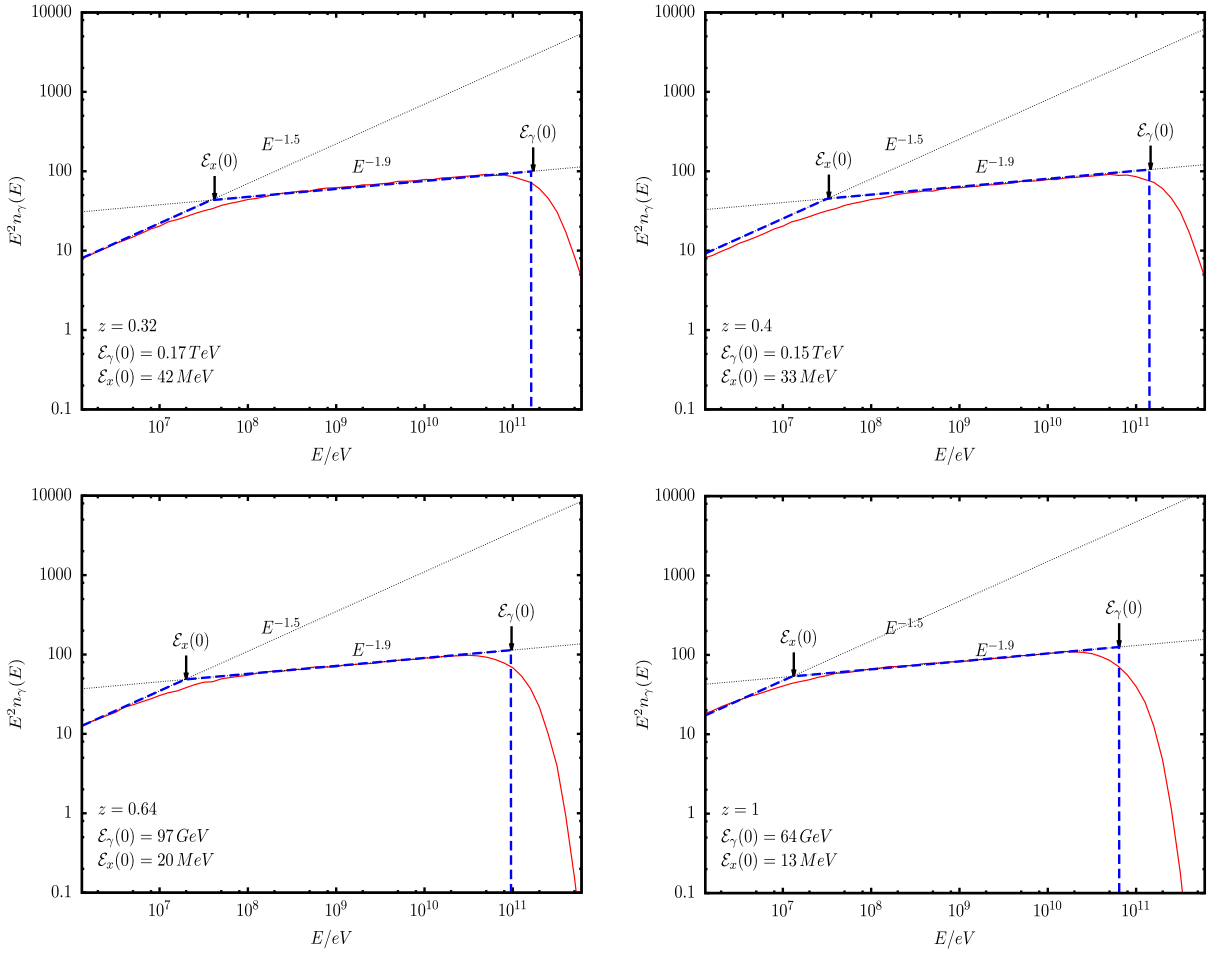

FIG. 4. Comparison of analytic calculations with numerical simulations from this work for large redshifts $z > 0.3$. Four panels show the comparison for redshifts 0.32, 0.4, 0.64, and 1.0 with the same notation as in Fig. 3 (see the text for details).

the fundamental spectrum of the cascade multiplication E^{-2} in analytic calculations (see Fig. 5).

D. Cascading only on CMB

This section has a technical character. Study of the cascade development only on CMB is important at least in two cases discussed in this paper:

(i) in the case of nearby sources when absorption of photons on EBL is absent.

(ii) in an expanding universe at large redshifts, when, due to high space density of CMB photons, a cascade is developing very fast with cutoff at $\mathcal{E}_\gamma^{\rm cmb} = m_e^2/\varepsilon_{\rm cmb}^z$; only later, the HE tail of the cascade photon distribution is slowly absorbed on EBL, followed by IC scattering of produced electrons and positrons on CMB photons.

Consider first cascading on *monochromatic CMB* at $z = 0$. The energy spectrum of the cascade is given again by Eq. (9) with

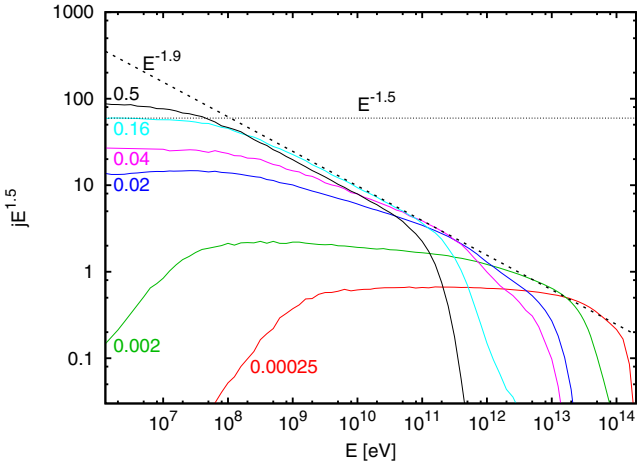

FIG. 5. Merging at increasing z of numerically simulated spectra to the universal $E^{-1.9}$ spectrum, which within the accuracy of calculations coincides with the fundamental cascade-multiplication spectrum $\propto E^{-2}$ in analytic calculations.

$$\mathcal{E}_\gamma = \mathcal{E}_\gamma^{\rm cmb} = m_e^2/\varepsilon_{\rm cmb} \approx 4.1 \times 10^{14}\ {\rm eV} \qquad (13)$$

and

$$\mathcal{E}_X = (4/3)(\mathcal{E}_e/m_e)^2\varepsilon_{\rm cmb} = (1/3)\mathcal{E}_\gamma^{\rm cmb}. \qquad (14)$$

The normalization is given by the same equation (10) with $\mathcal{E}_\gamma/\mathcal{E}_X = 3$ as follows from Eq. (14).

The remarkable feature of this calculation is the prediction of a very narrow cascade-multiplication energy width given by the ratio $\mathcal{E}_\gamma/\mathcal{E}_X = 3$, to be compared with 3×10^3 for the universal spectrum (9). This is the direct consequence of monochromatic CMB model accepted here (see the discussion in the end of this subsection).

For redshift z, there are two spectra of interest: the equilibrium spectrum at epoch z, $n_\gamma(E_\gamma, z)$ and this spectrum redshifted to epoch $z = 0$, $n_\gamma(E, 0)$.

Consider first the former. It is given by Eq. (9) with $\varepsilon_{\rm cmb}^z = \varepsilon_{\rm cmb}(1+z)$ and by characteristic energies at epoch z as

$$\mathcal{E}_\gamma(z) = m_e^2/\varepsilon_{\rm cmb}^z, \qquad \mathcal{E}_X(z) = (1/3)\mathcal{E}_\gamma(z). \qquad (15)$$

The normalization is given by Eq. (10) with $\mathcal{E}_\gamma(z)/\mathcal{E}_X(z) = 3$.

The spectrum redshifted to $z = 0$ may be also of interest for applications. It is given by redshifted characteristic energies $\mathcal{E}_\gamma(0) = \mathcal{E}_\gamma(z)/(1+z)$ and $\mathcal{E}_X(0) = \mathcal{E}_X(z)/(1+z)$,

$$\mathcal{E}_\gamma(0) = \frac{m_e^2}{\varepsilon_{\rm cmb}(1+z)^2} \qquad (16)$$

and

$$\mathcal{E}_X(0) = (1/3)\mathcal{E}_\gamma(0) = (1/3)\frac{m_e^2}{\varepsilon_{\rm cmb}(1+z)^2}. \qquad (17)$$

The redshift leaves constant K in normalization (10) invariant.

In fact, the monochromatic CMB model considered above is unrealistic and the introduction of the dichromatic model is necessary in most applications. It can be explained, for example, by cascading on the CMB at $z = 0$ at distance r from an observer. IC scattering occurs on all CMB photons and the average energy $\varepsilon_{\rm cmb} = 6.3 \times 10^{-4}$ eV may be safely assumed for all of them. However, the absorption of photons occurs on CMB photons from the high-energy tail of Planckian distribution, and the minimum energy of absorbed photons $\mathcal{E}_{\rm min}$ is determined by much higher energies of CMB photons $\tilde{\varepsilon}_{\rm cmb} \gg \varepsilon_{\rm cmb}$ as

$$\tilde{\mathcal{E}}_{\rm min} = \tilde{\mathcal{E}}_{\rm min}^{\rm cmb} = m_e^2/\tilde{\varepsilon}_{\rm cmb}. \qquad (18)$$

Energy $\tilde{\varepsilon}_{\rm cmb}$ coincides with the minimum energy in the HE tail of CMB photons for given E_γ because with the increasing of ε the number density of CMB photons exponentially falls down.

Therefore, we come back to the standard spectrum given by Eq (9) distorted at the highest energies due to the distortion of relation $E_\gamma = \frac{4}{3}\gamma_e^2\varepsilon_{\rm cmb}$ and with $\varepsilon_{\rm ebl}$ substituted everywhere by $\tilde{\varepsilon}_{\rm cmb}$.

E. Cascades from nearby sources

In this section, we calculate the cascade spectra, taking into account only CMB radiation and comparing them with numerical calculations with the same assumptions. This procedure clarifies the interesting physical details. As argued above, the cascade spectrum on the CMB only must be calculated using the dichromatic model of background radiation with $\varepsilon_{\rm cmb} = 6.3 \times 10^{-4}$ eV, which provides IC scattering, and higher-energy $\tilde{\varepsilon}_{\rm cmb}$, which provides the absorption of cascade photons with minimum energy $\tilde{\mathcal{E}}_{\rm min}$ given by Eq. (18). As far as physics is concerned, $\tilde{\varepsilon}_{\rm cmb}$ is minimal energy in the HE Planckian tail of photon distribution where the number density of photons is big enough enough for the absorption of photons with energy $\tilde{\mathcal{E}}_{\rm min}$. The energy $\varepsilon_{\rm min}$ for $\tilde{\mathcal{E}}_{\rm min}$ can be calculated from the kinematic relation for arbitrary E_γ and ε given by $E_\gamma\varepsilon(1+\cos\phi) = 2\varepsilon_{\rm cm}^2$, where ϕ is an angle between photons E_γ and ε in the laboratory system and $\varepsilon_{\rm cm}$ is the energy of each photon in the c.m. system. Finding the value ε from this relation for $E_\gamma = \tilde{\mathcal{E}}_{\rm min}$ and minimizing it with the choice $\cos\phi = 1$ and $\varepsilon_{\rm cm} = m_e$, we arrive at $\varepsilon_{\rm min} = m_e^2/\tilde{\mathcal{E}}_{\rm min}$ as in Eq. (18).

We can discuss now the spectra and basic features predicted for the cascades on the CMB from nearby sources, assuming tentatively, as the first step, $\varepsilon_{\rm cmb} \sim 6 \times 10^{-4}$ eV and $\tilde{\varepsilon}_{\rm cmb} \sim 2 \times 10^{-3}$ eV (these values will be determined more precisely after comparison with numerical simulations.)

The minimum absorption energy (on CMB photons) can be estimated from equation $\ell_{\rm abs}^{\rm cmb}(\tilde{\mathcal{E}}_{\rm min}) = r$, where $\ell_{\rm abs}^{\rm cmb}(E_\gamma)$ is the absorption length in the CMB background. It results in the well-known value $\tilde{\mathcal{E}}_{\rm min} \sim 1 \times 10^{14}$ eV, and it is given precisely, as $\tilde{\mathcal{E}}_\gamma$, for different distances r in Table I. Using Eq. (18), we find then $\tilde{\varepsilon}_{\rm cmb} \sim 2 \times 10^{-3}$ eV. The transition energy is given by $\mathcal{E}_X = (1/3)(\tilde{\mathcal{E}}_{\rm min}/m_e)^2\varepsilon_{\rm cmb}$, which approximately equal to 7×10^{12} eV. We cannot expect in this picture the standard spectra $\propto E^{-1.5}$ and $\propto E^{-2}$, especially the latter one. First of all, the spectrum can be flatter than $\propto E^{-2}$ due to the flattening of the $E_\gamma \propto E_e^{-2}$ regime in the end of the IC spectrum (see Fig. 2).

Another plausible reason is the width of the cascade-multiplication part of the spectrum, i.e., one with the conventional E^{-2} spectrum, but with the ratio $\mathcal{E}_\gamma/\mathcal{E}_X \approx 14$ to be compared with 3×10^3 for the case of the $(\varepsilon_{\rm cmb}, \varepsilon_{\rm ebl})$ background. The relatively small ratio

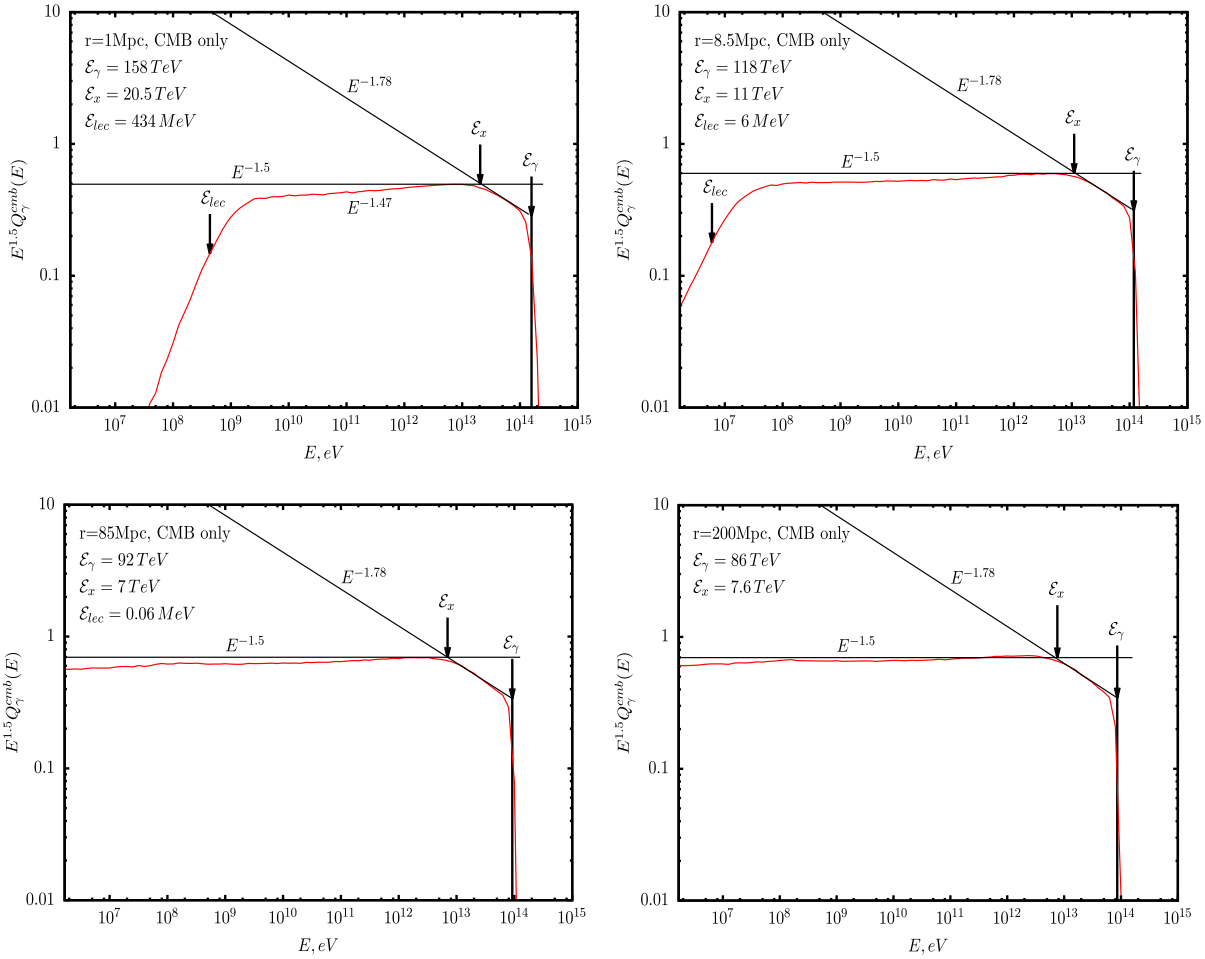

FIG. 6. Comparison of analytic calculations with numerical simulations for CMB radiation only for nearby sources at distances 1.0, 8.5, 85, and 200 Mpc.

$\mathcal{E}_\gamma/\mathcal{E}_X \approx 14$ is the reminiscent of the ratio 3 for the CMB monochromatic background model [see Eq. (14)]. Since the realistic simulations show a smooth transition between energies $\mathcal{E}_X$ and $\mathcal{E}_\gamma$, one may expect non-power-law of cascade-multiplication spectrum, in disagreement with the dichromatic model. As for the low-energy asymptotic spectrum $E^{-1.5}$, it also should be distorted, because absorption on $\tilde{\varepsilon}_{\rm cmb}$ photons occurs at distances of the order of the distance to the source r, and thus a cascade is underdeveloped. Now, we will compare the analytic estimates with accurate numerical simulations for cascades on CMB radiation and obtain more precisely parameters of our dichromatic model for different distances r to the source. We will change the notation as $\tilde{\mathcal{E}}_{\rm min} \equiv \tilde{\mathcal{E}}_\gamma$ to emphasize that this is the value of the spectrum cutoff.

As the first step, we find $\tilde{\mathcal{E}}_\gamma$ from equation $\ell_{\rm abs}^{\rm cmb}(\tilde{\mathcal{E}}_\gamma) = r$, where $\ell_{\rm abs}^{\rm cmb}(E_\gamma)$ is absorption length in the CMB background. The values of $\tilde{\mathcal{E}}_\gamma$ are shown in Table I for distances 1.0, 8.5, 85, and 200 Mpc.

Next, we calculate $\tilde{\varepsilon}_{\rm cmb}$ using Eq. (18) and values of $\tilde{\mathcal{E}}_{\rm min} \equiv \tilde{\mathcal{E}}_\gamma$ from Table I (third row).

The values of $\mathcal{E}_X$ in the fourth row are obtained from comparison with numerical simulations (see Fig. 6) as the intersection of the power-law approximation of the cascade-multiplication spectrum ($\propto E^{-1.8}$ in the Fig. 6) with the low-energy asymptotics.

The energies of the CMB photons $\varepsilon_{\rm cmb}$ (fifth row) are calculated using the equation $\mathcal{E}_X = (1/3)(\mathcal{E}_\gamma/m_e)^2\varepsilon_{\rm cmb}$.

In the last row of Table I, we put the low-energy cutoff $\mathcal{E}_{\rm lec}^\gamma$ of the cascade spectrum estimated in the following way.

The low-energy cascade electrons with energy below some critical energy $E_e^{\rm cr}(r)$ have a time of IC photon emission larger than the time-of-flight r/c. Therefore, radiation of IC photons with energies below $\mathcal{E}_{\rm lec}^\gamma = (4/3)(E_e^{\rm cr}/m_e)^2\varepsilon_{\rm cmb}$ is suppressed.

The critical energy of electron $E_e^{\rm cr}$ can be found from $\tau_e^{-1}(E_e^{\rm cr}) = c/r$, where $\tau_e(E)$ is the electron lifetime relative to the IC energy loss,

$$\tau_e^{-1}(E_e) = \left(\frac{1}{E_e}\frac{dE_e}{dt}\right)_{\rm IC} = \frac{4}{3}\sigma_T c\gamma_e \frac{\rho_{\rm cmb}}{m_e}, \qquad (19)$$

where σ_T is the Thompson cross section, $\gamma_e = E_e/m_e$ is the electron Lorentz factor, and $\rho_{\rm cmb} = \varepsilon_{\rm cmb} n_{\rm cmb}$ is the energy density of CMB radiation. Equation (19) can be rearranged as

$$\tau_e^{-1}(E_e) = \frac{4}{3}\sigma_T c n_{\rm cmb} \frac{E_e}{\mathcal{E}_\gamma^{\rm cmb}}, \tag{20}$$

where $\mathcal{E}_\gamma^{\rm cmb} = m_e^2/\varepsilon_{\rm cmb}$.

Using $\tau_e^{-1}(E_e^{\rm cr}) = c/r$, one finds the critical energy of electron $E_e^{\rm cr}$ and low-energy cutoff $\mathcal{E}_{\rm lec}^\gamma$ as

$$E_e^{\rm cr} = \frac{3/4}{\sigma_T n_{\rm cmb} r}\mathcal{E}_\gamma^{\rm cmb}; \qquad \mathcal{E}_{\rm lec}^\gamma = \frac{3}{4}\left(\frac{1}{\sigma_T n_{\rm cmb} r}\right)^2 \mathcal{E}_\gamma^{\rm cmb}. \tag{21}$$

From Table I, one can see that for nearby sources at distance 1–85 Mpc the dichromatic model is characterized by almost equal energies $\varepsilon_{\rm cmb} \approx 6 \times 10^{-4}$ eV and by similar values of $\tilde{\varepsilon}_{\rm cmb} \approx (2-3) \times 10^{-3}$ eV. For 200 Mpc, these values differ more considerably. The low-energy cutoff is observable only for very close sources $\mathcal{E}_{\rm lec}^\gamma \sim 400$ MeV for $r = 1$ Mpc; for $r = 8.5$ Mpc, it starts at 6 MeV.

Finally, we calculate the cascade-photon spectrum, taking the characteristic energy features from Table I and comparing this spectrum with precise numerical simulation on the CMB radiation only. One may expect that the canonical low-energy part of spectrum $\propto E^{-1.5}$ will survive for long-distance sources and may fail for short-distance ones, being underdeveloped. Figure 6 confirms this expectation; for distance $r = 200$ Mpc, the spectrum coincides well with the $E^{-1.5}$ shape and is weakly distorted at smaller distances. For the high-energy part of the spectrum $(\mathcal{E}_X - \mathcal{E}_\gamma)$, the energy interval is very short, and the spectrum is $\propto E^{-1.78}$ flatter than canonical 2.0.

III. NUMERICAL SIMULATIONS OF ELECTROMAGNETIC CASCADE PROPAGATION

In this section, we will discuss the basics of numerical simulations, the universality of EM cascade spectra in the numerical simulations, the calculated cascade energy spectra, and upper limits on the cascade energy density $\omega_{\rm cas}$ obtained from comparison of the calculated spectra with observations of Fermi LAT.

A. Generalities

The results presented in this work have been obtained with two independent numerical techniques, the Monte Carlo simulation and the code [36,37] based on the solution of Boltzmann kinetic equations for cascade particles propagation in one dimension. The latter method does not take into account deflections of cascade particles by the magnetic field and therefore is valid only for calculations with averaged angles and time or for diffuse fluxes. In Fig. 7, interaction and energy loss lengths are shown for electrons and photons. The lengths are defined as follows,

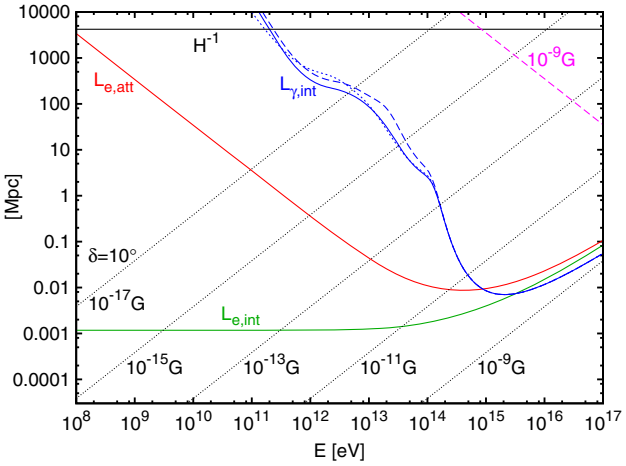

FIG. 7. Shown are the pair production interaction length [see Eq. (22)] calculated assuming EBL models of Ref. [16] (shown by the solid blue line), of Ref. [17] (dashed blue line), and of Ref. [40] (doted blue line); electron attenuation length [see Eq. (23)] due to inverse Compton scattering (red line) and the interaction length of this process (green line); 10° deflection length for electrons (shown by black dotted lines) for given values of the constant transverse component of the magnetic field; synchrotron energy loss length [see Eq. (28)] of electrons in $B_\perp = 10^{-9}$ G (shown by the pink dashed line); and adiabatic energy loss length (shown by the horizontal solid black line).

$$L_{\rm i,int}^{-1} = \int d\epsilon n(\epsilon) \int d\mu \frac{1-\beta_i\mu}{2}\sigma_i \tag{22}$$

$$L_{\rm e,att} = L_{\rm e,int} E_{\rm e}/\bar{E}_\gamma, \tag{23}$$

where $i = e, \gamma$; $\sigma_e = \sigma_{IC}$; $\sigma_\gamma = \sigma_{\rm PP}$; and $\bar{E}_\gamma$ is the mean energy of the recoil photon in IC. A number of kinetic equation-based codes has been developed at present (see, e.g., Refs. [36,38,39]). For the precise calculation of gamma-ray fluxes from individual sources in the presence of non-negligible magnetic fields, full 3D Monte Carlo simulation is needed. Such calculations as a rule require excessive computing time since the number of secondary particles grows exponentially in the cascade. In the Monte Carlo code used in this work, to speed up computations, we utilize, following Ref. [35], the weighted sampling of the cascade development. It allows us reduce the number of secondary particles.

While IC scattering occurs mostly on the CMB, the e^+e^- pair production, when it is below threshold on the CMB, takes place on infrared and optical components of EBL, which is not precisely known. A number of different models have been proposed for EBL [16,17,40–44]. There are some upper bounds on EBL in the literature that were based on observations of distant blazars. These limits are derived without taking into account the possible contribution of cosmic rays, and therefore these bounds can be relaxed [45]. The limits based on GRBs [46] remain

unaffected. The model of Ref. [43] is disfavored by the Fermi LAT observation of the photons from GRB 090902B and GRB 080916C. Note that limits based on GRB observations constrain only the highest-energy part of EBL. To obtain the range of $\omega_{\rm cas}$ in this work, we use the baseline model from the recent work [40], which includes estimates of EBL for redshifts $z \leq 10$. In addition, we use for comparison the "best-fit" and "lower-limit" models of Refs. [16,17], providing estimates of EBL for $z \leq 5$. The EBL model of Ref. [42] for $z \leq 2$ is used only for comparison of our numerical calculations with Ref. [29].

Another poorly known factor which is crucial for consideration of the electromagnetic cascades from individual sources is intergalactic magnetic field (IGMF). Even in the presence of relatively weak IGMF, the angular size of sources can increase due to the deflection of electrons and positrons moving along the curved trajectories with curvature radius R_c,

$$R_c = \frac{E_e}{eB} \simeq 1.1 \left(\frac{E_e}{1\ \mathrm{TeV}}\right)\left(\frac{B_\perp}{10^{-15}\ \mathrm{G}}\right)^{-1} \mathrm{Mpc}. \quad (24)$$

After traversing distance L, the misalignment of the electron direction with the primary gamma-ray direction is given by angle δ,

$$\delta \simeq \begin{cases} \frac{L}{R_c}, & L \ll \lambda_B \\ \frac{\sqrt{L\lambda_B}}{R_c}, & L \gg \lambda_B, \end{cases} \quad (25)$$

where λ_B is IGMF correlation length. In the second case above, many stochastic deflections were taken into account. The deflections in the cascade cannot be neglected as soon as electron energy-loss length becomes comparable with the defocusing length, i.e., the travel path at which electrons are deflected by maximal angle δ. The definition of δ varies for different problems. It may be related to the experimental angular resolution or average angular distance between the sources. The defocusing lengths for $\delta = 10°$ and a range of IGMF strengths (assuming $\lambda_B \gg L$) are shown in Fig. 7 (black dashed lines) together with the energy-loss length (red curve) for comparison. As an example in the case $B = 10^{-15}G$ and $\delta = 10°$, one can infer that deflections become important for electron energy $E_{\rm e} \lesssim 1$ TeV, which corresponds to the typical recoil photon energy of 3 GeV. Below this energy, gamma-ray flux is essentially isotropized.

Current theoretical and observational constraints on the IGMF mean value and correlation length are summarized in the review [22] as

$$10^{-17}\ \mathrm{G} \lesssim B \lesssim 10^{-9}\ \mathrm{G}, \quad (26)$$

$$\lambda_B \gtrsim 1 pc, \quad (27)$$

where the obtained lower limit on IGMF is based on the simultaneous observation of GeV and TeV gamma radiation from the hard-spectrum blazars RGB J0710+591, 1ES $0229+200$, and 1ES $1218+304$ (Fermi/LAT observations in GeV and Veritas, Major Atmospheric Gamma Imaging Cherenkov Telescope, and High-Energy Stereoscopic System observations in TeV) [29].

In the special case of IGMF being close to its upper limit $B \simeq 10^{-9}$ and for the sources emitting ultrahigh-energy photons or electrons with $E \gtrsim 10^{19}$ eV, the electron synchrotron losses should be taken into account. The pink line on Fig. 7 represents the energy-loss length for this process given by [47]

$$L_{\rm syn}^{-1} = \frac{1}{E_{\rm e}}\frac{dE_{\rm e}}{dt} = -\frac{4}{3}\sigma_T \frac{B^2}{8\pi}\frac{E_{\rm e}}{m_{\rm e}^2}, \quad (28)$$

where σ_T is the Thomson cross section and m_e is the electron mass. In this paper, we disregard the synchrotron energy losses if not otherwise stated.

B. Comparison

In this section, we compare the cascade spectra obtained using the kinetic equation and Monte Carlo codes from the present work with other numerical simulations and with analytic calculations. Figure 8 demonstrates the level of agreement between our numerical calculations, simulation [29], and analytic calculation for a source at $z = 0.13$ injecting 10^{14} eV photons and using the EBL model of Ref. [42] for photon absorption. One may see in this figure the familiar two cascade energy spectra $\propto E^{-1.5}$ and $\propto E^{-1.9}$ and also the steeper high-energy feature in good agreement in all three numerical simulations. As will be

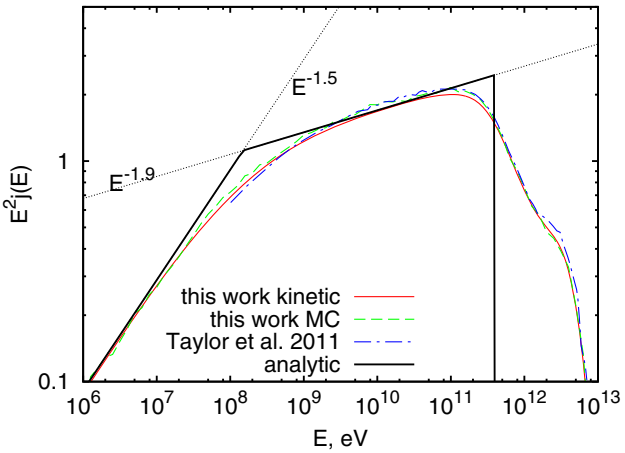

FIG. 8. Average cascade spectrum obtained using the kinetic equation code (solid curve) and Monte Carlo code (dashed curve) compared with analytic calculation and with results of Monte Carlo simulation [29] (dot-dashed curve), all for the injection of 10^{14} eV photons at $z = 0.13$.

demonstrated below, this feature plays an important role in the determination of the cascade energy density $\omega_{\rm cas}$.

The diffuse gamma-ray spectrum as presented by Fermi LAT in 2015 [7] shows the steepening which starts at 1×10^{11} eV and continues as a more sharp cutoff at $\epsilon=2.5\times10^{11}$ eV. Both the high-energy features in theoretical spectra in Fig. 8, $\propto E^{-1.9}$ and more steep feature above it, are flatter than that observed by Fermi LAT, and it results in the upper limit on $\omega_{\rm cas}$. The reason may be easily understood from Fig. 8.

For given large enough $\omega_{\rm cas}$, the realistic, numerically calculated, spectra from Fig. 8 can intersect the Fermi high-energy tail at some energy. It means that at energy above the crossing the calculated cascade flux is larger than the measured Fermi flux. To eliminate this contradiction, one must lower the calculated cascade flux, i.e., $\omega_{\rm cas}$. This procedure results in the upper limit on $\omega_{\rm cas}$.

The case of analytic spectrum in Fig. 8 is quite different. It has a sharp cutoff at $\epsilon_\gamma\approx400$ GeV close to the Fermi cutoff energy $\epsilon\approx250$ GeV, and thus a quite larger $\omega_{\rm cas}$ is allowed.

All effects which make lower the high-energy cutoff in the calculated cascade spectrum, e.g., high redshift of production, *increase* the upper limit on $\omega_{\rm max}$.

IV. UNIVERSALITY OF THE CASCADE SPECTRA IN NUMERICAL SIMULATIONS

Universality of the cascade energy spectrum was discovered first in analytic calculations [33], and we will start our discussion from the analytic dichromatic model of Sec. II A. This universality is clearly seen from Eq. (9), where two joint energy spectra $\propto E^{-3/2}$ and $\propto E^{-2}$ appear, divided by two boundary energies $\mathcal{E}_X$ and $\mathcal{E}_\gamma$, built from basic parameters of dichromatic model $\varepsilon_{\rm cmb}$ and $\varepsilon_{\rm ebl}$. The main features of this universal spectrum include: (i) The same energy shape of the spectrum produced by initial photon/electron if its primary energy is sufficiently high. Ultimately the scale can be as high as $E_0\gtrsim m_e^2/\varepsilon_{\rm cmb}\sim0.4$ PeV, and it is the basic one in analytic calculations. The lower universality scale $E_0\sim100$ TeV is found in numerical simulations, and this result is very natural and may be expected *a priori*. In the analytic approach, the cutoff energy $\mathcal{E}_\gamma^{\rm cmb}=0.4$ PeV is a consequence of the monochromatic spectrum of CMB photons $\epsilon_{\rm cmb}=6.3\times10^{-4}$ eV. In numerical simulations, absorption occurs on the high-energy tail of Planckian distribution of CMB photons and absorption produced at $\mathcal{E}_\gamma^{\rm cmb}\approx100$ TeV when $\ell_{\rm abs}$ reaches c/H_0. (ii) The cascade energy spectrum is the same for any injection spectrum $Q(E_s)$ at $E_s\gtrsim E_0$ (in other words, the cascade spectrum forgets what injection spectrum produced it). (iii) The cascade spectrum does not depend on distance to the point where the cascade started. (iv) The energy density of the cascade $\omega_{\rm cas}$ is the only cascade characteristic which determines the spectrum.

These properties of "analytic" cascades will be referred to as *strong universality*.

For realistic cascades in the expanding universe, the strong universality, as it is formulated above, is not valid. The cascade spectrum observed at $z=0$ depends on the redshift of production z_s, e.g., due to the dependence $\mathcal{E}_X$ and $\mathcal{E}_\gamma$ on z_s and simply due to the redshift of the spectrum. Consider, for example, the generation rate of photons/electrons in an expanding universe in the form $Q(E_s,z_s)=\phi(E_s)R(z_s)$ with E_s above the universality scale E_0. All cascades produced at fixed redshift z_s have the same cascade spectrum $q_{\rm cas}(E)$ at $z=0$. However, cascades originating at different z_s have the different cascade spectra at $z=0$, and integration over z_s results in cascade spectra, which depend on the distribution of production rate $Q(E_s,z_s)$ over z_s. The predicted cascade spectrum is determined not only by $\omega_{\rm cas}$ but, e.g., by parameters of the cosmological evolution of the sources. Universality of the cascade spectra remains only for a subclass of the sources with approximately equal redshifts. In summary, the sources in the expanding universe with the generation rate $Q(E_s,z)$, with E_s above the universality scale E_0 and with arbitrary dependence on z [e.g., evolution $(1+z)^m$ up to $z_{\rm max}$] have the following properties of universality: (i) The energy shape of the EM cascade at $z=0$ is independent from E_s or from injection spectrum $\phi(E_s)$; i.e., for fixed z_s, the shape is the same for different E_s, or for different spectra $\phi(E_s)$. (ii) The cascade spectrum at $z=0$ is not uniquely determined by $\omega_{\rm cas}$ but depends also on the evolution of $Q(E,z)$ with z, e.g., through parameters m and $z_{\rm max}$. (iii) A subclass of the sources with the same (or almost the same) redshift z_s has the identical cascade spectrum at $z=0$, which is characterized by the single parameter $\omega_{\rm cas}$.

This case can be referred to as *weak universality*.

The class of sources with the fixed redshift of production z_s, i.e., with production rate $Q(E_s,z)=\phi(E_s)\delta(z-z_s)$, has all the properties of strong universality, except iii, and can be attributed to strong universality for arbitrary generation spectrum $\phi(E_s)$ with E_s above the universal scale E_0. The corresponding cascade spectrum is characterized by a single parameter $\omega_{\rm cas}$ for any fixed z_s.

Consider z-fixed sources in some details, starting from low initial energy $E_s<E_0$. While increasing E_s the $z=0$ cascade spectrum evolves to a strongly-universal spectrum, reaching it at scale E_0 and remains unchanged. Figure 9 illustrates this statement. The figure presents the diffuse fluxes generated by the population of sources with the fixed energy of injected photon E_s and with fixed redshift z_s. The diffuse spectrum *shape* at $z=0$ does not depend on E_s as long as $E_s\gtrsim\mathcal{E}_\gamma^{\rm cmb}$. In fact, for remote enough sources at $z\gtrsim0.1$, universality is reached at the scale $E_0\gtrsim100$ TeV. This observation was tested for all EBL models used in this work.

The numerically calculated diffuse cascade spectra from the sources with fixed redshift z_s and energy E_s are shown in Figs. 9a–9c. The spectra are expected to be strongly

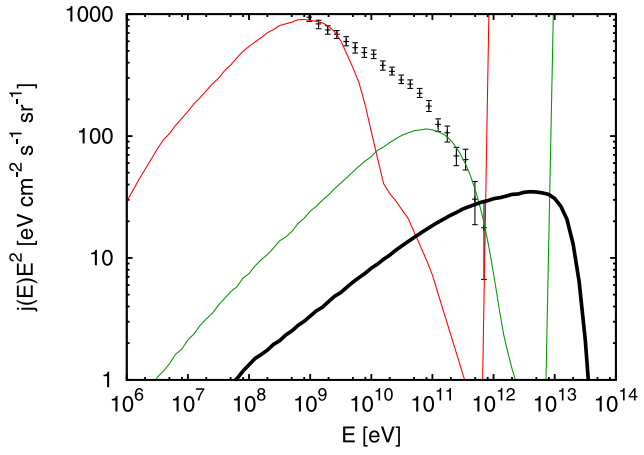

(a) $z_s = 0.01$

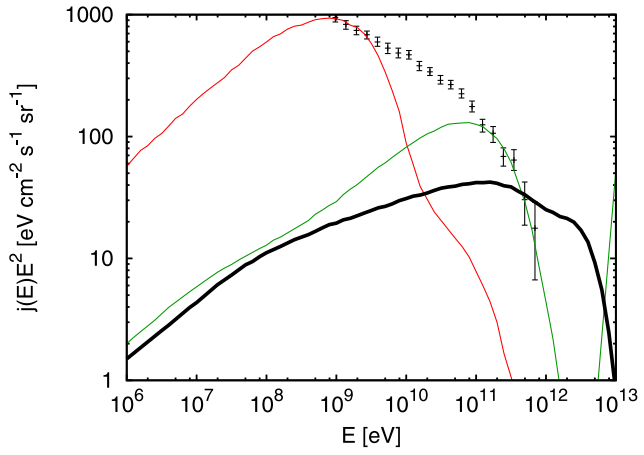

(b) $z_s = 0.1$

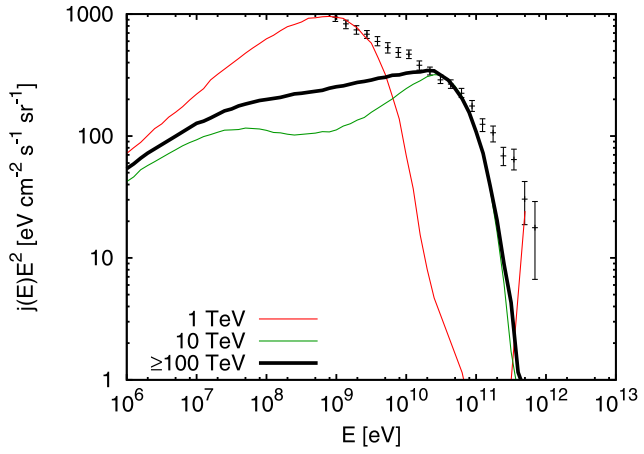

(c) $z_s = 1$

FIG. 9. Diffuse cascade spectrum from sources injecting photons with energy $E_s = 1$ TeV (red curves), 10 TeV (green curves), and $E_s \geq 100$ TeV (black thick curves) at redshifts $z = 0.01$, $z = 0.1$, and $z = 1$. Photon fluxes are limited from above by the Fermi EGB flux, shown by black error bars, with foreground model B [7]. The curves obtained for initial photon energies greater than 100 TeV coincide in all figures. In calculations, the EBL flux from Ref. [40] is used.

universal when energy E_s exceeds the largest scale $E_0 = \mathcal{E}_\gamma^{\rm cmb} = 0.4$ PeV. All three figures (a), (b), and (c) demonstrate that the spectra are universal at $E \geq E_0$, where $E_0 = 100$ TeV. This energy can be considered as the energy scale of universality in numerical simulations (see the discussion above). Apart from identical spectra, they have at large $z_s \geq 0.1$ the predicted standard spectrum $\propto E^{-3/2}$ at low energy, $\propto E^{-1.9}$, at intermediate energies with highest-energy feature in the end of the spectrum (cf. Fig. 8). The spectra with $E_s = 100$ TeV (black thick curves) and with all energies $E_s \gtrsim 100$ TeV are indistinguishable in Figs. 9.

The cascade universality makes it hard to extract the injection spectrum from the diffuse spectrum observed at $z = 0$. On the other hand, the comparison of the calculated and observed spectra allows us to estimate the upper limit on the main characteristic of the universal cascade spectrum, the cascade energy density $\omega_{\rm cas}$ at $z = 0$. This problem will be considered in the next section.

V. UPPER LIMIT ON $\omega_{\rm cas}$ FROM FERMI LAT DATA

The upper limit on the cascade energy density given by Eq. (1) as 5.8×10^{-7} eV/cm^3 was derived in Ref. [34] from the first-year Fermi data [6]. Here, we obtain this limit from 50 months Fermi LAT observations [7] using a somewhat different approach.

Fermi LAT [6] presents two kinds of extragalactic gamma-ray fluxes in energy range 100 MeV—820 GeV: extragalactic gamma-ray background (EGB) and isotropic diffuse gamma-ray background (IGRB). EGB presents the total extragalactic gamma-ray flux, from which about half is given by the resolved individual sources. In the cascade calculations, we use these fluxes to normalize the upper limits on the cascade energy density $\omega_{\rm cas}$. The highest and most conservative upper limit on the theoretical energy density $\omega_{\rm cas}$ is imposed by Fermi EGB flux and is marked as $\omega_{\rm cas}^{\rm tot}$. In the isotropic case, the estimate of $\omega_{\rm cas}^{\rm iso}$ can be obtained from Fermi IGRB flux [7] assuming additionally highly homogeneous distribution of gamma-ray sources or astrophysical gamma-ray generation scenarios in which the IGMF must be high enough to isotropize the cascade electrons and positrons (or their parent particles) in the space.

EGB flux is higher than IGRB, and the two calculated values of $\omega_{\rm cas}$ follow this hierarchy. Both fluxes are described by the power-law spectrum with index $\gamma \approx 2.3$ and with a steeper highest-energy tail starting at $E_{\rm cut} = \epsilon \approx 250$ GeV (beginning of the steepening). The nature of the gamma-ray flux above $E_{\rm cut}$ is not well known, but we consider it a diffuse flux. This high-energy steep component (tail) is responsible for a stronger upper limit on $\omega_{\rm cas}$ in comparison with an earlier paper [8]. The realistic, numerically calculated, spectra in Fig. 8 are flatter than the

highest-energy Fermi tail and can intersect it at some energy (see Sec. III B).

A. Upper limit on $\omega_{\rm cas}$ in analytic calculations

To illustrate our method of calculating $\omega_{\rm cas}$, we will consider first a simple example of the analytic model, followed by the accurate numerical calculations.

Consider the energy of the Fermi IGRB spectrum cutoff $\epsilon = 2.5 \times 10^5$ MeV, where the measured flux is $J_\gamma^{\rm igrb} = 4.80 \times 10^{-16}$ cm^{-2} s^{-1} sr^{-1} MeV^{-1}. We use here the analytic dichromatic model with $\varepsilon_{\rm cmb} = 6.3 \times 10^{-4}$ eV and $\varepsilon_{\rm ebl} \approx 1$ eV, which provides the high-energy cutoff in the cascade spectrum $\mathcal{E}_\gamma = m_e^2/\varepsilon_{\rm ebl} = 2.61 \times 10^5$ MeV, practically the same as that observed in the Fermi IGRB spectrum $\epsilon = E_{\rm cut}$. We take the cascade spectrum as $J_{\rm cas}(E) \propto E^{-1.9}$ at $\mathcal{E}_X \le E \le \mathcal{E}_\gamma$ and $E \propto E^{-1.5}$ at $E \le \mathcal{E}_X$. Then, the cascade energy density can be calculated using the cascade flux $J_{\rm cas}(E)$ as

$$\omega_{\rm cas} = \frac{4\pi}{c}\left(\int_0^{\mathcal{E}_X} dEEJ_{\rm cas}(E) + \int_{\mathcal{E}_X}^{\mathcal{E}_\gamma} dEEJ_{\rm cas}(E)\right). \quad (29)$$

The most restrictive relation we use in the calculation of Eq. (29) is given by the cascade flux in the energy interval $\mathcal{E}_X \le E \le \mathcal{E}_\gamma$,

$$J_{\rm cas}(E) = J_{\rm igrb}(\epsilon)(E/\epsilon)^{-1.9}, \quad (30)$$

which includes the normalization of the cascade flux by Fermi IGRB flux $J_{\rm igrb}$ at energy $\epsilon = E_{\rm cut}$. This particular condition provides the low upper limit on $\omega_{\rm cas}$ in this estimate.

For the interval $E \le \mathcal{E}_X$, we use

$$J_{\rm cas}(E) = J_{\rm igrb}(\epsilon)(\mathcal{E}_X/\epsilon)^{-1.9}(E/\mathcal{E}_X)^{-1.5}. \quad (31)$$

As a result, we obtain the upper limit on the energy density of cascade radiation,

$$\omega_{\rm cas} \le 6.6\frac{4\pi}{c}\epsilon^2 J_{\rm igrb}(\epsilon) = 8.3 \times 10^{-8}\ {\rm eV/cm^3}, \quad (32)$$

to be compared with the much larger cascade upper limit $\omega_{\rm cas}^{\rm max} = 5.8 \times 10^{-7}$ eV/cm^3 obtained in Ref. [8] and used in Ref. [9]. The reason is that for the normalization of the calculated flux we used the measured flux at energy $\epsilon = 2.5 \times 10^5$ MeV, which is located below the Fermi $E^{-2.3}$ approximation of the flux. However, this argument implies the further decrease of $\omega_{\rm cas}^{\rm max}$. In more realistic numerical simulations, there is the high-energy tail (see Fig. 8), and the intersection of this tail with the steep high-energy Fermi IGRB tail demands lowering the calculated flux, i.e., further suppression of $\omega_{\rm cas}$. Another reason for the modification of the calculated spectrum is connected with the interpretation of the two highest-energy points in the Fermi LAT spectrum above 2.5×10^5 MeV. If these points belong to isotropic diffuse radiation, the high-energy theoretical tail must be shifted downward, and it results in the lowering of $\omega_{\rm cas}$. However, in case the weak universality $\omega_{\rm cas}$ is not the only parameter which influences the flux, it could be that other parameters, e.g., the cosmological evolution of the sources, can shift the flux upward at the same $\omega_{\rm cas}$.

The stronger upper limit on $\omega_{\rm cas}^{\rm iso}$ obtained here puts the stronger upper limit on the flux of UHE extragalactic protons and cosmogenic neutrinos, in comparison with Refs. [8–10]. The effect of increasing the fraction of resolved sources [48] diminishes further $J_{\rm cas}(E)$ and $\omega_{\rm cas}$ given above.

B. Upper limit on $\omega_{\rm cas}$ in numerical simulations

Now, we will proceed to the consideration of $\omega_{\rm cas}$ using the calculation of the cascade spectra in numerical simulations, kinetic equations, and Monte Carlo. These calculations provide us with the shape of the cascade spectra at $E < \epsilon_\gamma$, and normalization by the observed Fermi LAT spectrum allows us to obtain the values of $\omega_{\rm cas}$, the final aim of our research in this paper.

Below, we calculate $\omega_{\rm cas}^{\rm tot}$ and $\omega_{\rm cas}^{\rm iso}$ for two cases: (i) the redshift-fixed photon-electron sources with very-high-energy E_s and (ii) redshift-distributed sources with the injection rate of photons/electrons $Q(E_s, z)$ smoothly dependent on z. Case i results in strong universality, and ii, for the general case of z dependence, results in weak universality. The scale of very high energy is given by $E_s \gtrsim \mathcal{E}_\gamma^{\rm cmb} \gtrsim 0.4$ PeV for analytic calculations, though as argued above and as Figs. 9(a)–9(c) show, the universal shape of the spectra is reached already at energy scale $E_s \sim 100$ TeV.

Let us now come over to the numerical calculation of the cascade spectra and to the evaluation of $\omega_{\rm cas}$. We consider two cases:

(i) the redshift-fixed and energy-fixed sources with injection rate

$$Q(E, z) \propto \delta(z - z_s)\delta(E - E_s), \quad (33)$$

(ii) redshift-distributed sources with injection rate

$$Q(E, z) = (1 + z)^{3+m}\delta(E - E_s), \quad \text{at } z < z_{\rm max}, \quad (34)$$

with $1 < z_{\rm max} < 5$ and $0 < m < 5$ (the case $m = 0$ corresponds to a constant source density in the comoving frame).

In calculations for both cases, we will keep $E_s \ge 100$ TeV to provide universality.

The calculated spectra will be normalized by Fermi LAT spectra, EGB, and IGRB. The highest and most conservative upper limit on energy density $\omega_{\rm cas}$ is imposed directly by EGB flux, which includes also the flux of resolved extragalactic discrete sources. To be even more conservative, we take the fluxes of EGB (and IGRB, too) as a maximal one allowed by systematic uncertainties. Using these two fluxes, we obtain the upper limits on $\omega_{\rm cas}^{\rm igrb}$ and $\omega_{\rm cas}^{\rm egb}$; the latter will be considered as maximally allowed $\omega_{\rm max}$.

Case i spectra are shown for three values of z_s in Figs. 9(a)–9(c). At energies E_s higher than 100 TeV, all spectra are the same. Figure 10 presents the cascade spectra for continuous source distribution (34), which illustrates the dependence of the cascade spectra on evolution parameters m and $z_{\rm max}$.

From Fig. 10, one may observe that spectra with low $z_{\rm max} = 1$ have large cutoff energy $E_{\rm max}$, and to avoid the contradiction with Fermi data, one must shift the calculated spectrum downward, thus diminishing $\omega_{\rm cas}$.

Spectra with large $z_{\rm max} = 5$ have lower $E_{\rm max}$ due to the redshift factor $(1+z)$ and respectively larger $\omega_{\rm cas}$. Dependence on m works in a similar way. Figure 10 allows us to calculate $\omega_{\rm cas}$ using the corresponding curves. As a result, the constraints on the energy density of cascades with large m and $z_{\rm max}$ are relaxed.

We already have seen such an effect in Sec. II B for the case of the analytic solution with the sharp high-energy cutoff, which starts at low energy (see Fig. 8). Now, we can generalize the both cases, formulating what will be called the "$E_{\rm max}$ rule" used here and below. It reads: Increasing $E_{\rm max}$ in the calculated cascade spectrum suppresses $\omega_{\rm cas}$. Indeed, Fig. 10 shows that increasing $E_{\rm max}$ needs the lowering of the total curve $J(E)$ to avoid the excess of the predicted flux $J(E)$ over the observed Fermi flux. For changing $E_{\rm max}$, one may use, for example, the cosmological evolution: increasing $z_{\rm max}$ results in decreasing $E_{\rm max}$ at $z = 0$ by a factor $(1+z)$.

Another feature observed in Fig. 10 is the standard energy spectra $\propto E^{-1.5}$ transforming to $\propto E^{-1.9}$ at higher energy (see these curves in the figure).

In Fig. 11, we present the maximum cascade energy density $\omega_{\rm cas}^{\rm iso}$ consistent with the Fermi IGRB flux and $\omega_{\rm cas}^{\rm tot}$ consistent with the Fermi EGB flux [7] for two cases of source distribution (33) and (34). To obtain these quantities, we normalize the cascade spectrum calculated in numerical simulations by IGRB or EGB fluxes [7].

In panel (a), we show the energy density $\omega_{\rm cas}^{\rm tot}$ and $\omega_{\rm cas}^{\rm iso}$ calculated in the model with fixed redshift of the source z_s and with fixed energy E_s of the primary photon/electron. This is the case of strong universality, when the cascade

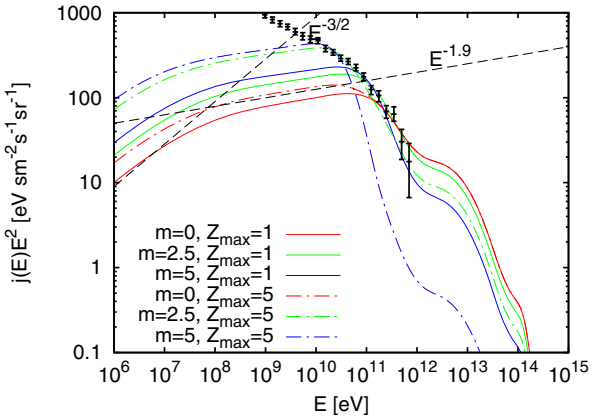

FIG. 10. Cascade spectra for source distribution (34), with $E_s = 1$ PeV, with various m and $z_{\rm max}$, and with the EBL model of Ref. [16]. The spectra are normalized by the Fermi LAT EGB flux (with foreground model B) [7] shown by black error bars.

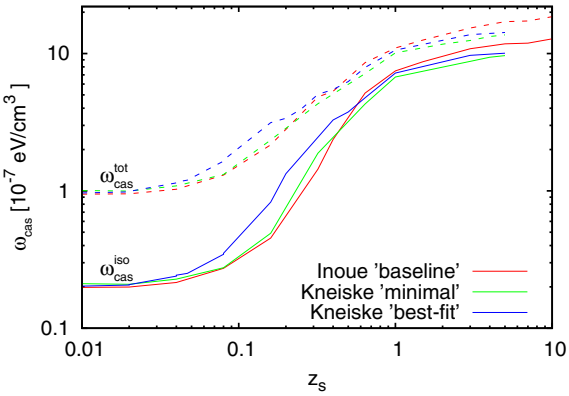

(a) sources at fixed z

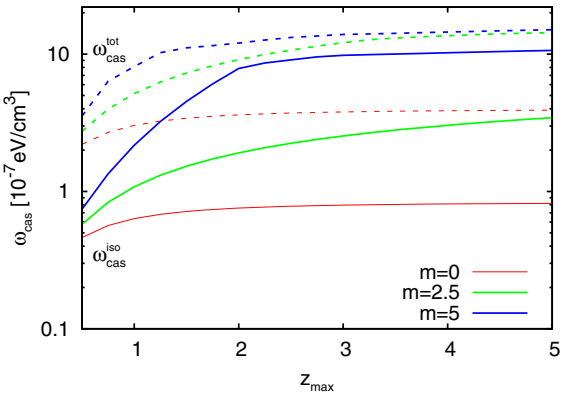

(b) sources distributed in z

FIG. 11. Upper limits on the cascade energy density $\omega_{\rm cas}$ obtained for source distribution with fixed z_s, Eq. (33) (panel a), and with continuous z_s distribution, Eq. (34) (panel b). The total upper limits $\omega_{\rm cas}^{\rm tot}$ are obtained using Fermi EGB flux (dashed lines), and isotropic upper limits $\omega_{\rm cas}^{\rm iso}$ are obtained using Fermi IGRB flux (full lines). The various EBL models are used in simulations shown in panel (a): Ref. [40] (red lines), Ref. [16] (blue lines), and Ref. [17] (green lines). In the lower panel (b), the EBL model of Ref. [40] is used.

spectrum is determined by a single parameter $\omega_{\rm cas}$. Uncertainties, caused by different EBL models, are not large, and values of $\omega_{\rm cas}^{\rm tot}$ are larger than $\omega_{\rm cas}^{\rm iso}$, as expected. The values of $\omega_{\rm cas}(z)$ at large z exceed that at small z according to the $E_{\rm max}$ rule: large z gives small $E_{\rm max}$, and small $E_{\rm max}$ results in large flux and hence in large $\omega_{\rm cas}$. One can see this effect in Fig. 11(a).

In Fig. 11(b), the case of more realistic continuous z distribution, as given by Eq. (34), is presented. It is described by weak universality, when the cascade spectrum depends, apart from $\omega_{\rm cas}$, on other parameters, in particular on parameters of cosmological evolution m and $z_{\rm max}$. The low z and large z regimes exist here, too, being provided by the $E_{\rm max}$ rule.

The lowest, $\omega_{\rm cas}^{\rm iso} = 4 \times 10^{-8}$ eV/cm^3, is obtained for $z_{\rm max} \lesssim 1$ and for the absence of evolution $m = 0$. It is an order of magnitude lower than the limit 5.8×10^{-7} eV/cm^3 found in Ref. [8] for the secondary photons produced during the propagation of UHECR. The limit appears very restrictive for fluxes of protons in the UHECR and cosmogenic neutrinos produced at $z_{\rm max} \lesssim 1$ and in the absence of evolution $m = 0$.

Nonevolutionary models with m $= 0$ and $z_{\rm max} \gtrsim 2$ have $\omega_{\rm cas}^{\rm iso} \leq 8 \times 10^{-8}$ eV/cm^3 (see Fig. 11, panel b) which allows some of nonevolutionary UHECR proton models from Table 1 of Ref. [34]. The models with strong evolution $m = 5$ and $z_{\rm max} \gtrsim 2$ allow large $\omega_{\rm cas}^{\rm iso} \approx 8 \times 10^{-7}$ eV/cm^3, favorable for UHECR proton models with strong evolution and large $z_{\rm max}$.

The smallness of $\omega_{\rm cas}$ produced in cosmic-ray models in comparison with $\omega_{\rm cas}^{\rm iso}$ measured by Fermi LAT is not the only criterion for a successful cosmic-ray model. It must satisfy another more sensitive criterion: not to exceed the Fermi IGRB flux in the highest-energy bin (in fact, this criterion enters the comparison of energy densities as an integral characteristic). Unfortunately, the IGRB flux estimate in the highest-energy bin is strongly model dependent and suffers from low statistics. We have considered problem of survival of UHECR proton models in details in a separate work, emphasizing the role of the highest-energy bin (in preparation). This problem was already studied in the works [8–10] and most recently in a different approach in Ref. [49].

The above analysis is based on EGB and IGRB fluxes derived using 50 months of Fermi-LAT observation [7]. The two recent catalogs of sources which appeared later [50] and [51] may have an effect on the IGRB estimate and therefore on our results. These catalogs are based on the new program of analysis, Pass 8, with the improved reconstruction and classification of events and with the time of observation increased to 6 years. The analysis of the work [48] shows that the considerable fraction of high-energy events above 50 GeV can be attributed to unresolved sources, most of which are blazars. For EGB flux, contribution of blazars according to this work reaches $86^{+16}_{-14}\%$. This implies a stronger bound on the true isotropic flux. This effect can be roughly described by inequality

$$\omega_{\rm cas}^{\prime\rm iso} \lesssim 0.28 \omega_{\rm cas}^{\rm tot}. \tag{35}$$

VI. SUMMARY

Using both an analytic approach and numerical simulations, we have described the development of electromagnetic cascades in the universe in the presence of CMB and EBL background radiations. The cascades develop due to IC scattering on the most numerous CMB photons $e + \gamma_{\rm cmb} \to e' + \gamma'$ and pair production on less numerous EBL photons $\gamma + \gamma_{\rm ebl} \to e^- e^+$. A primary particle below is called the photon, though the electron is implied under this name, too.

For analytic calculations, we use dichromatic model with fixed energy of CMB photons $\varepsilon_{\rm cmb} = 6.3 \times 10^{-4}$ eV and EBL photons with $\varepsilon_{\rm ebl} = 0.68$ eV. In the cascade photon spectrum there are two characteristic energies: absorption energy $\mathcal{E}_\gamma^{\rm ebl} \sim m_e^2/\varepsilon_{\rm ebl}$ and Inverse Compton energy of a photon $\mathcal{E}_X = (1/3)(\mathcal{E}_\gamma/m_e)^2 \varepsilon_{\rm cmb}$, produced by an electron/positron which is born in $\gamma + \gamma_{\rm ebl}$ collision. Thus, in the analytic dichromatic model, we have

$$\mathcal{E}_\gamma^{\rm ebl} = \frac{m_e^2}{\varepsilon_{\rm ebl}} = 3.9 \times 10^{11} \text{ eV}$$
$$\mathcal{E}_X = \frac{1}{3} \mathcal{E}_\gamma^{\rm ebl} \frac{\epsilon_{\rm cmb}}{\epsilon_{\rm ebl}} = 1.2 \times 10^8 \text{ eV}. \tag{36}$$

The cascade initiated at large distance by a very-high-energy photon/electron has a spectrum given by Eq. (9), which is $\propto E^{-3/2}$ in the low-energy regime $E \lesssim \mathcal{E}_X$, with $\propto E^{-2}$ at intermediate energies $\mathcal{E}_X \lesssim E \lesssim \mathcal{E}_\gamma$ and with a high-energy cutoff at $\mathcal{E}_\gamma$, where $\mathcal{E}_\gamma$ numerically can differ from $\mathcal{E}_\gamma^{\rm ebl}$ in Eq. (36) due to different values of $\epsilon_{\rm ebl}$.

The numerical simulations confirm the analytic spectrum with index $\gamma_1 = 3/2$ being exact, $\gamma_2 = 2$ being approximate ($\gamma_2 \approx 1.9$ in numerical simulations), and with a sharp high-energy cutoff for a source at a very large distance. The artificially sharp energy transitions in the analytic spectrum at $E = \mathcal{E}_X$ and $E = \mathcal{E}_\gamma$ appear in numerical simulations as continuous transition features. This is the most important difference between the analytic solution and more precise numerical simulation.

The remarkable feature found in both analytic and numerical solutions is the *universality* of the cascade spectrum. In the analytic solution, the strong universality is seen explicitly from the spectrum given by Eq. (9), where the shape of the spectrum does not depend on the initial energy of the primary photon at $E_s > E_0$ nor on the distance to observer r, unless it is too small. The energy scale of universality is $E_0 = \mathcal{E}_\gamma^{\rm cmb} = 0.4$ PeV. The energy $\mathcal{E}_X$ which separates two regimes, $\propto E^{-3/2}$ and $\propto E^{-2}$, and

the energy of spectrum cutoff $\mathcal{E}_\gamma$ are built from the main physical constants of the model [see Eq. (5)], and the cascade energy spectrum does not depend on variables of the model, in particular on initial energy E_s and the distance to the source r. The main features of this universality, specific for the analytic model developed in Sec. II A, are (i) the same energy shape of the cascades produced by the primary photon/electron if its energy E_s is larger than universality scale E_0, (ii) the same cascade energy spectrum for any injection spectrum $Q(E)$ at $E \geq E_0$ (in other words, the cascade spectrum forgets what injection spectrum produced it), (iii) indepedence of the spectrum shape from the distance to the point where the cascade started, and (iv) the energy density of the cascade $\omega_{\rm cas}$ as the only cascade parameter which determines the spectrum shape.

These properties of analytic cascades are referred to as strong universality.

For realistic cascades in the expanding universe, property i is modified as follows: cascades initiated at the fixed redshift z by the photon/electron with sufficiently high-energy $E_s > E_0$ turn at $z = 0$ into cascades with a spectrum independent of E_s but dependent on z. These spectra are calculated by numerical simulation. Property ii remains almost the same: cascade spectra initiated at the same z with different injection spectra $Q(E)$ are almost identical. However, if injection spectrum $Q(E, z)$ smoothly changes with z, the total diffuse spectrum obtained by integration over z is not universal; the spectra are different for a different dependence of $Q(E, z)$ on z. The diffuse spectra for various $Q(E, z)$ are determined in this case not only by $\omega_{\rm cas}$ but also by other parameters from $Q(E, z)$ distribution.

We refer to the case described above as weak universality. Some of the described properties of these cascades, studied in numerical simulations, are shown in Fig. 9.

The main aim of this paper is to obtain the upper limit on the cascade energy density $\omega_{\rm cas}$ using the Fermi LAT flux of gamma radiation. In the analytic model with strong universality, there is the direct and transparent method which allows us to obtain a strong enough upper limit on the cascade energy density. This upper limit follows from Eq. (29) and results in $\omega_{\rm cas} \leq 8.3 \times 10^{-8}$ eV/cm^3. The specific property of this limit is the high-energy cutoff, i.e., $E_{\rm max}$, given by $\mathcal{E}_\gamma = m_e^2/\varepsilon_{\rm ebl}$, which at $\varepsilon_{\rm ebl} \sim 1$ eV coincides with cutoff energy in Fermi IGRB spectrum. The limit is stronger if the model-dependent $E_{\rm max} = \mathcal{E}_\gamma$ is higher.

An even stronger upper limit is obtained comparing the *numerical calculations* of the cascade energy shape with the Fermi measured spectrum, due to its high-energy tail. If the calculated spectrum crosses the steep high-energy Fermi tail at $E_{\rm cross}$, the calculated flux above $E_{\rm cross}$ exceeds the observations. To eliminate this contradiction, one must lower the total calculated spectrum decreasing $\omega_{\rm cas}$, and thus we arrive at the $E_{\rm max}$-rule formulated in Sec. V B as increasing $E_{\rm max}$ in the calculated spectrum further suppressing $\omega_{\rm cas}$.

In particular, the $E_{\rm max}$ rule works efficiently in evolutionary $(1+z)^m$ models with large m and large $z_{\rm max}$. Since the flux in these models is dominated by production at $z_{\rm max}$, the maximum energy $E_{\rm max}$ at $z = 0$ becomes $(1 + z_{\rm max})$ times less, and, respectively, $\omega_{\rm cas}$ is allowed to be higher, as one observes in Fig. 11(b).

We describe now the obtained limits on $\omega_{\rm cas}$ in some details.

Fermi LAT presented two kinds of measured extragalactic fluxes: the total EGB and IGRB. The corresponding energy densities obtained, using EGB and IGRB as the upper limits, are $\omega_{\rm cas}^{\rm tot}$ and $\omega_{\rm cas}^{\rm iso}$, respectively, the former being always larger. Both fluxes, EGR and IGRB, have systematic and statistical uncertainties and are to some extent model dependent (e.g., foreground models). To be conservative, we use maximal fluxes allowed within these uncertainties.

The both spectra, EGR and IGRB, have steepening, which starts at $E_{\rm cut} = 250$ GeV, and at higher energies become steeper. The method of $\omega_{\rm cas}$ calculation is mainly based on this steep high-energy feature.

The shape of the cascade spectrum is accurately calculated using kinetic equations and MC methods. As these calculations show, $E_{\rm max}$ in the cascade spectrum at $z = 0$ becomes smaller at larger z_s of cascade production. Since the flux of EGR/IGRB is $J(E) \propto E^{-3.2}$, small $E_{\rm max}$ results in larger flux $J(E_{\rm max})$, i.e., in larger $\omega_{\rm cas}$. In other words, $\omega_{\rm cas}$ is rising with increasing z_s as we see indeed in Fig. 11(a).

Figure 11(a) shows the case of fixed z_s, when strong universality holds, and thus the $\omega_{\rm cas}$ value is unique for each z_s. As expected, $\omega_{\rm cas}^{\rm tot}$ is larger than $\omega_{\rm cas}^{\rm iso}$. For small distances $z_s < 0.1$, cascades are underdeveloped, and $\omega_{\rm cas}$ are small: $\omega_{\rm cas}^{\rm iso} \lesssim (2-3) \times 10^{-8}$ eV/cm^3. At large $z_s \gtrsim 1$, the energy density is larger: $\omega_{\rm cas}^{\rm iso} \gtrsim (5-8) \times 10^{-7}$ eV/cm^3. These results depend weakly on models of EBL.

The strong dependence of $\omega_{\rm cas}$ on redshift z_s in Fig. 11(a) implies the dependence of the energy density on the source distribution over z, seen in Fig. 11(b). One may observe there an increase of $\omega_{\rm cas}$ with $z_{\rm max}$ up to $z_{\rm max} \sim 1$, with the constant value at larger $z_{\rm max}$. This constant value depends on cosmological evolution $(1+z)^m$. One may summarize the values of $\omega_{\rm cas}^{\rm iso}$ as 5×10^{-8} eV/cm^3 in the case of the absence of cosmological evolution $m = 0$ and up to 9×10^{-7} eV/cm^3 in the case of strong cosmological evolution $m = 5$.

The large $\omega_{\rm cas}^{\rm max}$ allowed in the case of strong evolution with large $z_{\rm max}$ is explained by the diminishing of $E_{\rm max}$ by the factor $(1 + z)$ in the cascade spectrum at $z = 0$.

The first results of Fermi LAT [6] demonstrated [8–10] that cascade energy density $\omega_{\rm cas} \approx 5.8 \times 10^{-7}$ eV/cm^3 excludes some proton models of UHECR and cosmogenic neutrinos. However, some models survived. The

new data of Fermi LAT [7] discovered the steep energy feature in the end of the spectrum, which further constrains the cascade energy density. The new limit is model dependent. For models with strong universality of the cascade spectrum, the limits on $\omega_{\rm cas}$ became stronger, and restrictions on UHECR became more severe. However, for the models with weak universality, the restrictions are relaxed. In particular, the evolutionary models with strong evolution and large $z_{\rm max}$ the energy density can be larger than 6×10^{-7} eV/cm^3, i.e., larger than the previous limit.

ACKNOWLEDGMENTS

Work of O. K. was supported by the Russian Science Foundation, Grant No. 14-12-01340. O. K. is grateful to GSSI and LNGS for hospitality.

[1] A. A. Penzias and R. W. Wilson, Astrophys. J. **142**, 419 (1965).
[2] K. Greisen, Phys. Rev. Lett. **16**, 748 (1966); G. T. Zatsepin and V. A. Kuzmin, Pis'ma Zh. Eksp. Teor. Fiz. **4**, 114 (1966) [JETP Lett. **4**, 78 (1966)].
[3] V. S. Beresinsky and G. T. Zatsepin, Phys. Lett. B **28**, 423 (1969); Sov. J. Nucl. Phys. **11**, 111 (1970).
[4] V. S. Berezinsky and A. Yu. Smirnov, Astrophys. Space Sci. **32**, 461 (1975).
[5] P. Sreekumar *et al.*, Astrophys. J. **494**, 523 (1998).
[6] A. A. Abdo *et al.* (Fermi-LAT Collaboration), Phys. Rev. Lett. **104**, 101101 (2010).
[7] M. Ackermann *et al.* (Fermi-LAT Collaboration), Astrophys. J. **799**, 86 (2015).
[8] V. Berezinsky, A. Gazizov, M. Kachelrieß, and S. Ostapchenko, Phys. Lett. B **695**, 13 (2011).
[9] M. Ahlers, L. A. Anchordoqui, M. C. Gonzalez-Garcia, F. Halzen, and S. Sarkar, Astropart. Phys. **34**, 106 (2010).
[10] G. B. Gelmini, O. Kalashev, and D. V. Semikoz, J. Cosmol. Astropart. Phys. 01 (2012) 044.
[11] O. F. Prilutsky, Ph.D. thesis, Moscow Engineering Institute, 1972.
[12] A. W. Strong, A. W. Wolfendale, and J. Wdowczyk, Nature (London) **241**, 109 (1973).
[13] R. J. Gould and D. Schreder, Phys. Rev. Lett. **16**, 252 (1966).
[14] V. Berezinsky, Yad. Fiz. **11**, 399 (1970) [, Sov. J. Nucl. Phys. **11**, 399 (1970)].
[15] F. A. Aharonian, P. S. Copi, and H. J. Völk, Astrophys. J. Lett. **423**, L5 (1994).
[16] T. M. Kneiske, K. Mannheim, and D. H. Hartmann, Astron. Astrophys. **386**, 1 (2002); **413**, 807 (2004).
[17] T. M. Kneiske and H. Dole, Astron. Astrophys. **515**, A19 (2010).
[18] A. Neronov and D. V. Semikoz, JETP Lett. **85**, 473 (2007).
[19] P. P. Kronberg, Rep. Prog. Phys. **57**, 325 (1994).
[20] D. Grasso and H. R. Rubinstein, Phys. Rep. **348**, 163 (2001).
[21] R. M. Kulsrud and E. G. Zweibel, Rep. Prog. Phys. **71** 046901, (2008).
[22] R. Durrer and A. Neronov, Astron. Astrophys. Rev. **21**, 62 (2013).
[23] L. Biermann, Z. Naturforsch. **5**, 65 (1950).
[24] L. Mestel and D. L. Moss, Mon. Not. R. Astron. Soc. **204**, 557 (1983).
[25] M. V. Medvedev and A. Loeb, Astrophys. J. **526**, 697 (1999).
[26] F. Miniati and A. R. Bell, Astrophys. J. **729**, 73 (2011).
[27] A. Elyiv, A. Neronov, and D. V. Semikoz, Phys. Rev. D **80**, 023010 (2009).
[28] A. Neronov and L. Vovk, Science **328**, 73 (2010).
[29] A. M. Taylor, I. Vovk, and A. Neronov, Astron. Astrophys. **529**, A144 (2011).
[30] H. Tashiro, W. Chen, F. Ferrer, and T. Vachaspati, Mon. Not. R. Astron. Soc. **445**, L41 (2014).
[31] W. Chen, B. D. Chowdhury, F. Ferrer, H. Tashiro, and T. Vachaspati, Mon. Not. R. Astron. Soc. **450**, 3371 (2015).
[32] G. R. Blumenthal and R. J. Gould, Rev. Mod. Phys. **42**, 237 (1970).
[33] V. S. Berezinsky, S. V. Bulanov, V. A. Dogiel, V. L. Ginzburg, and V. S. Ptuskin, *Astrophysics of Cosmic Rays* (Elsevier, Amsterdam, 1990); *originally in Russian* (Nauka, Moscow, Russia, 1984).
[34] V. Berezinsky, A. Gazizov, M. Kachelrieß, and S. Ostapchenko, Phys. Lett. B **695**, 13 (2011).
[35] M. Kachelriess, S. Ostapchenko, and R. Tomas, Comput. Phys. Commun. **183**, 1036 (2012).
[36] O. K. Kalashev, PhD thesis, Institute for Nuclear Research Russian Academy of Sciences, 2003; O. E. Kalashev and E. Kido, J. Exp. Theor. Phys. **120**, 790 (2015).
[37] G. B. Gelmini, O. Kalashev, and D. V. Semikoz, J. Cosmol. Astropart. Phys. 01 (2012) 044.
[38] S. Lee, Phys. Rev. D **58**, 043004 (1998).
[39] S. Yoshida, G. Sigl, and S.-j. Lee, Phys. Rev. Lett. **81**, 5505 (1998).
[40] Y. Inoue, S. Inoue, M. A. R. Kobayashi, R. Makiya, Y. Niino, and T. Totani, Astrophys. J. **768**, 197 (2013).
[41] J. R. Primack, R. C. Gilmore, and R. S. Somerville, AIP Conf. Proc. **1085**, 71 (2008); J. D. Finke, S. Razzaque, and C. D. Dermer, Astrophys. J. **712**, 238 (2010).
[42] A. Franceschini, G. Rodighiero, and M. Vaccari, Astron. Astrophys. **487**, 837 (2008).
[43] F. W. Stecker, M. A. Malkan, and S. T. Scully, Astrophys. J. **648**, 774 (2006).
[44] F. W. Stecker, M. A. Malkan, and S. T. Scully, Astrophys. J. **761**, 128 (2012); S. T. Scully, M. A. Malkan, and F. W. Stecker, Astrophys. J. **784**, 138 (2014).

[45] W. Essey, O. Kalashev, A. Kusenko, and J. F. Beacom, Astrophys. J. **731**, 51 (2011).
[46] A. A. Abdo *et al.*, Astrophys. J. **723**, 1082 (2010).
[47] For a standard textbook discussion, see J. D. Jackson, *Classical Electrodynamics*, 2nd ed. (Wiley, New York, 1975).
[48] M. Di Mauro (Fermi-LAT Collaboration), arXiv: 1601.04323.
[49] R. Y. Liu, A. M. Taylor, X. Y. Wang, and F. A. Aharonian, arXiv:1603.03223.
[50] F. Acero *et al.* (Fermi-LAT Collaboration), Astrophys. J. Suppl. Ser. **218**, 23 (2015).
[51] M. Ackermann *et al.* (Fermi-LAT Collaboration), Astrophys. J. Suppl. Ser. **222**, 5 (2016).